Reduced systemic autophagy by simultaneous loss of ATG4B, ATG4C and ATG4D leads to accelerated aging in mice

Gemma G. Martínez-García[1,2,3], María F. Suárez[3], Mª Del Mar Rodríguez-Santamaria[3], David Roiz-Valle[2,3,4], Clea Bárcena[2,4], Andrés Corrochano-Ruiz[1,2,3], Isaac Tamargo-Gómez[1,2,3], Pablo Mayoral[2,3,4], Aurora Astudillo[2,3,5], Christina Sveen[6], Nikolai Engedal[6], Carlos López-Otín[4,7,8], Álvaro F. Fernández[2,3,4] and Guillermo Mariño[1,2,3]

[1]Departamento de Biología Funcional, Facultad de Medicina, Universidad de Oviedo, Spain; [2]Instituto Universitario de Oncología (IUOPA); [3]Instituto de Investigación Sanitaria del Principado de Asturias (ISPA); [4]Departamento de Bioquímica y Biología Molecular, Universidad de Oviedo, Spain; [5]Biobanco del Principado de Asturias (BBPA_ISPA_IUOPA). Registro nacional de Biobancos PT20/161. [6]Department of Tumor Biology, Institute for Cancer Research, Oslo University Hospital, Montebello, N-0379 Oslo, Norway. [7]Facultad de Ciencias de la Vida y la Naturaleza, Universidad Nebrija, Madrid, Spain; [8]Centre de Recherche des Cordeliers, Sorbonne Université, INSERM U1138, Paris, France.

Send correspondence to:
Guillermo Mariño
Departamento de Biología Funcional
Facultad de Medicina, Universidad de Oviedo
33006 Oviedo-SPAIN
Autophagy and Metabolism Lab,
Instituto de Investigación Sanitaria del Principado de Asturias (ISPA)
33010 Oviedo-Spain
Tel. 34-646554011;
E-mail: marinoguillermo@uniovi.es

ABSTRACT

Autophagy is a housekeeping catabolic process crucial for maintaining cell, tissue and organism functions. Through the years, the study of animal models with tissue-specific inactivation of autophagy essential genes has allowed us to understand its protective roles in the context of multiple human diseases, including cancer and neurodegeneration. However, due to the essential nature of autophagy, the effects of its systemic inhibition in mammals have not been explored in detail. Here, we report the generation of ATG4A-only mice, simultaneously deficient for three of the four mammalian ATG4 proteases (ATG4B, ATG4C and ATG4D). Through extensive characterization of ATG4A-only cells, which show a severe (albeit not complete) deficiency in autophagic activity, we define the specific roles of ATG4A protease towards ATG8 proteins (its physiological substrates), shedding some light into the evolutionarily-acquired complexity of mammalian ATG4-ATG8 system. Moreover, we show that the profound whole-body autophagy deficiency of ATG4A-only mice not only impacts the function of multiple tissues, but also leads to the development of an accelerated aging phenotype, characterized by the accumulation of genetic damage, systemic senescence, and premature death. Thus, through the analysis of ATG4A-only mice and other murine models deficient for ATG4 proteases, we not only provide new insights on how autophagy maintains cell, tissue, and organismal homeostasis, but also show for the first time that the degree of autophagic competency ultimately emerges as a critical determinant of organismal longevity.

INTRODUCTION

In the last years, our knowledge of autophagy has vastly improved, providing evidence on how this housekeeping catabolic process is crucial for the maintenance of a wide variety of essential cell functions in all nucleated cells. In this regard, the generation of cellular and animal models deficient for autophagy genes has proven pivotal for elucidating new evolutionarily acquired roles for this pathway in multicellular organisms. In mammalian cells, several essential autophagy genes, such as *Atg3*, *Atg5*, *Atg7, Ambra1, FIP200* and *Becn1* among others, operate in a non-redundant way in central hubs of the autophagic pathway, meaning that their knockout causes a complete (and lethal) defect in autophagy. Due to this reason, the consequences of gene targeting either through a whole-body approach or through the generation of tissue-specific knockout models for these genes usually result in a major impact on the function of the tissue or cell type in which autophagy has been disrupted (1, 2). These approaches have yielded extensive and valuable information into the general and specific functions of autophagy in different animal models, including laboratory mice. However, the dramatic consequences of total autophagy disruption in mammals might have precluded the elucidation of the physiological functions of this pathway. Similarly, the effects of systemically reduced autophagy have been addressed by very few studies due mainly to the lack of appropriate animal models. This is a relevant question, as it is known that autophagic potential progressively declines as the organism ages (3), and some environmental factors, including pollutants or nanoparticles, interfere with components of the pathway, reducing autophagic competency in a progressive way (4). Not surprisingly, autophagy dysregulation is one of the essential drivers for the loss of proteostasis, one of the main hallmarks of aging (5, 6).

In contrast to the former cases, mammals possess several orthologues for the yeast protease gene Atg4 (which is essential for autophagy in this simple organism), namely ATG4A, ATG4B, ATG4C and ATG4D (7). The activity of these proteases is required for the autophagy-related functions of their physiological substrates, which are the mammalian orthologs of yeast Atg8, termed LC3A, LC3B, LC3C (only in human cells), GABARAP, GABARAPL1 and GABARAPL2, collectively known as mATG8s. Among the four mammalian ATG4 proteases, ATG4B is the main responsible for the initial proteolytic activation of mATG8 proteins, except for GABARAPL2 (8, 9). This cleavage is strictly required for their subsequent lipidation, creating phosphatidyl ethanolamine-conjugated mATG8s that associate with autophagosomes (10). In contrast, ATG4D is the main responsible for the delipidation of these mATG8 proteins from autophagic membranes, once autophagosome maturation is complete (11). The function of ATG4C is complementary to that of ATG4D (12) and the physiological function of ATG4A is currently unknown. Given some degree of functional redundancy in the ATG4 family, the knockout of one single member of the ATG4 protease family is compatible with a close-to-normal development before and beyond birth (13, 14). For instance, mice deficient for ATG4C show only mild-tissue-specific alterations in autophagic degradation, being otherwise indistinguishable from their wild-type (WT) counterparts (12). By contrast, mice deficient for ATG4B are viable but exhibit a significant reduction

of their autophagic potential in multiple distinct organs. Thus, autophagic flux, as well as the depletion of the autophagic substrate p62/SQSTM, are diminished in both fed and starved *atg4b*$^{-/-}$ mice compared to WT littermates. When unchallenged, the limited autophagic competency of *atg4b*$^{-/-}$ mice is sufficient to achieve a lifespan almost identical to that of WT mice with no higher incidence of pathologies. However, *atg4b*$^{-/-}$ mice are not able to mount an appropriate autophagic response upon autophagy-inducing stimuli, which contributes to an increased susceptibility to diverse experimentally-induced pathologies, including bleomycin-induced pulmonary fibrosis, lung injury during endotoxemia, susceptibility to experimental colitis, cellular damage upon optic nerve transection, obesity and other metabolic disturbances, among others (15-20). Mice deficient for ATG4D have also been recently generated. These mice develop late-onset cerebellar neurodegeneration and although they show alterations in the status of some autophagy-relevant parameters, due to the preponderant role of ATG4D in mATG8s delipidation, do not show any alteration in autophagic flux.

Here, we report the generation and analysis of mice triple deficient for these three proteases ATG4B/C/D (ATG4A-only), which therefore only express ATG4A from the ATG4 family. Through the study of ATG4A-only mice cells and tissues, we are able to define the molecular functions of ATG4A protease towards mATG8 proteins when no other member of the ATG4 protease family is expressed. Moreover, we characterize the effect of ATG4B/C/D triple deficiency in autophagy regulation and execution, both in mice tissues and cultured cells. Finally, through the phenotypical analysis of triple knockout (ATG4A-only) mice, we are able to describe for the first time that a drastic and systemic reduction of autophagy, but not its total impairment, leads to the development of multiple aging-related features and to the accumulation of DNA-damage, inflammation and senescence markers, similar to those found in murine models of accelerated aging, which together result in dramatically-reduced lifespan.

MATERIALS AND METHODS

Mice strains

ATG4A-only mice were generated at the University of Oviedo facilities by crossing previously generated *atg4b*$^{-/-}$(21) *atg4c*$^{-/-}$(12) and *atg4d*$^{-/-}$(11) mice.

Cell lines

The different mouse embryonic fibroblasts (MEF) lines that were used in this work were generated as follows: MEFs were extracted from E13 embryos. Embryos were sterilized with ethanol, washed with PBS, and triturated with razor blades. Samples were then incubated in DMEM (Gibco) overnight at 37ºC and 5% CO_2. The next day, cultured cells were trypsinized, filtered and washed. Finally, MEFs were incubated at 37ºC and 5% CO_2 and used for the corresponding experiments. These MEFs were maintained in Dulbecco's modified Eagle's medium (DMEM) supplemented with ×1 non-essential amino-acids, 10 mM HEPES buffer, 100 µM 2-mercaptoethanol, ×1 sodium pyruvate and 10% fetal bovine serum. HEK293T cells were maintained in DMEM supplemented with 10% fetal bovine serum, 1% penicillin-streptomycin-l-glutamine and 1% antibiotic-antimycotic (Gibco) at 37°C in 5% CO2.

Antibodies

In this study, the following antibodies were used:

Anti-SQSTM1 (M01, clone 2C11) (Abnova Corporation, Cat# H00008878-M01); anti-LC3A (Proteintech, Cat# 12135-1-AP); anti-LC3B (Novus, Cat# NB600-1384); anti-GABARAP (MBL International, Cat# PM037); anti-GABARAPL1 (ATG8L) (Proteintech, Cat# 11010-1-AP); anti-Atg4A (Arigo, ARG54904 and Thermo Scientific, PA557632); anti-GABARAPL2 (GATE-16) (MBL International, Cat# PM038); anti-beta-Actin (Sigma-Aldrich, Cat# A2228); Alexa Fluor® 488 goat anti-mouse (Invitrogen, Ref.#A-11001); Alexa Fluor® 488 goat anti-rabbit (Invitrogen, Ref.#A-11008); Alexa Fluor® 532 goat anti-mouse (Invitrogen, Ref.#A-11002); Alexa Fluor® 532 goat anti-rabbit (Invitrogen Ref.#A-11009); anti-alpha-Tubulin (Sigma-Aldrich, Cat# T5168); anti-GAPDH (Novus Cat# NB300-320); anti-ubiquitin (FK2) (Enzo Life Sciences, Cat# BML-PW8810-0500); anti-LAMP-1 (H4A3) (Santa Cruz Biotechnology, Cat# sc-20011); anti-FIP200 (D10D11) (Cell Signaling Technology, Cat# 12436); anti-ULK1 (D8H5) (Cell Signaling Technology, Cat# 8054); anti-Phospho-ULK1 (Ser555) (D1H4) (Cell Signaling Technology, Cat# 5869); anti-phospho-ULK-1 (Ser757) (D7O6U) (Cell Signaling Technology, Cat# 14202); anti-Atg101 (E1Z4W) (Cell Signaling Technology, Cat# 13492); anti-Atg13 (D4P1K) (Cell Signaling Technology, Cat# 13273); anti-ATG14/Barkor (C-Terminal) (Proteintech, Cat# 24412-1-AP); anti-Beclin-1 (Cell Signaling Technology, Cat# 3738); anti-Atg12 (Cell Signaling Technology, Cat# 2011); anti-p70 S6 Kinase (Cell Signaling Technology, Cat# 9202); anti-Phospho-p70 S6 Kinase (Thr421/Ser424) (Cell Signaling Technology, Cat# 9204); anti-4E-BP1 (Cell Signaling Technology, Cat# 9452); Anti-AMPK-alpha (Cell Signaling Technology, Cat# 2532); anti-Phospho-AMPK (Thr172) (Cell Signaling Technology, Cat# 2531); anti-NBR1 (Cell

Signaling Technology, Cat# 9891); anti-NDP52 (D1E4A) (Cell Signaling Technology, Cat# 60732); anti-OPTN (Proteintech, Cat# 10837-1-AP).

Plasmids and recombinant vectors

In this study, the following plasmids were used:

pCI-neo-myc-LC3 (deltaC22) (Addgene_45448); pMXs-IP-EGFP-ULK1 (Addgene_38193); pMXs-IP-EGFP-mAtg5 (Addgene_38196); pMRXIP-GFP-Stx17TM (Addgene_45910); pMRXIP GFP-VAMP8 (Addgene_45919); pBABE-puro SV40 LT (Addgene_38193); pMXs-IP-EGFP-hAtg13 (Addgene_38191); pMXs-IP-EGFP-LC3 (Addgene_38195); pMXs-puro GFP-p62 (Addgene_38277). Other plasmids appearing in the paper which are not listed here were generated at our lab and are fully available upon request to the corresponding author.

Other reagents

Other reagents and chemicals used in this study were:

Bafilomycin A1 (Enzo Life Science, Cat# BML-CM110-0100, CAS: 88899-55-2); Torin 1 (Selleckchem, Cat# S2827, CAS:1222998-36-8); 3-Methyladenine (Sigma Aldrich, Cat# M9281, CAS: 5142-23-4); 2-mercaptoethanol (Merck, Ref.# 8057401000, CAS 60-24-2); 2-Propanol (Merck, Ref.#1096341000, CAS 67-63-0); 30% polyacrylamide solution, 37.5:1 (Bio-Rad, Ref.# 1610159, CAS 0079-6-1 and 868-63-3); Ammonium Acetate (Merck, Ref.# 1011151000, CAS 631-61-8); Ammonium persulfate (Bio-Rad, Ref.# 1610700, CAS 7727-54-0); cOmpleteTM (Roche, Ref.# 11873580001); DAPI (Sigma, Ref.# D9542, CAS 28718-90-3); DMEM (Sigma, Ref.# D5796-24X500ML); dNTPs (Invitrogen, Ref.# 10297018); DPBS 10x (Invitrogen, Ref.# 14200-083); Earle's balanced salt solution (Invitrogen, Ref.# 24010-043); EDTA disodium salt (Affymetrix, Ref.# 156971KG, CAS 6381-92-6); EDTA tetrasodium salt dihydrate (Affimetrix, Ref.#157001KG, CAS 10378-23-1); Lipofectamine® (Invitrogen, Ref.# 18324-012); Opti-MEM (Invitrogen, Ref.# 31985-062); Paraformaldehyde solution (Merck, Ref.# 1.04002.1000, CAS 50-00-0 and 67-56-1); PEG8000 (Sigma, Ref.# P2139-1KG, CAS 25322-68-3); Pen-Strep-Glut (Invitrogen, Ref.# 10378-016); PhosSTOP (Roche, Ref.# 4906837001); Platinum Taq DNA polymerase (Invitrogen, Ref.#10966-034); Polybrene (Santa Cruz, Ref.# sc-134220, CAS 28728-55-4); Proteinase K (Roche, Ref.# 03115879001, CAS 39450-01-6); Puromycin dihydrochloride (Gibco, Ref.# a11138-03, CAS 58-58-2); RNase A (Qiagen, Ref.# 19101, CAS 9001-99-4); RNaseOUT (Invitrogen, Ref.# 10777-019); Sodium dodecyl sulfate (Merck, Ref.# 8220501000, CAS 151-21-3); Super Script® IV Reverse Transcriptase (Invitrogen, Ref.#18090050); TEMED (Affymetrix, Ref.# US76320-100GM, CAS 110-18-9); ThremoScriptTM RNase H (Invitrogen, Ref.#12236-022); TRizol® (Ambion, Ref.#15596018); Trypsin-EDTA (0.05%) (Gibco, Ref.# 25300-054); Tween-20 (Sigma-Aldrich, Ref.#P1379-1L, CAS 9005-64-5); Sodium pyruvate (Invitrogen, Ref.# 11360-039); MEM NEAA (Invitrogen, Ref.# 11140-035); HEPES buffer (Invitrogen, Ref.# 15630-056).

Lentiviral transduction of MEF cells

Transfections were carried out in cells seeded onto gelatinized coverslips and using Lipofectamine, following the manufacturer's instructions. For lentiviral infection, HEK-293T cells were transfected with lentiviral vector together with packaging plasmids psPAX2 and pMD2.G using Lipofectamine. After 48 hours of transfection, supernatants were filtered through 0.45 µm polyethersulfone filters to collect the viral particles and added at 1:3 dilution to previously seeded mouse fibroblasts supplemented with 0.8 µg/ml of polybrene. Selection with puromycin (2 µg/mL) was performed 2 days after infection.

Quantitative real-time PCR

cDNA was synthesized using 1 to 5 µg of total RNA, 0.14 mM oligo (dT) (22-mer) primer, 0.2 mM concentrations each of deoxynucleoside triphosphate and SuperScript II reverse transcriptase (Invitrogen). Quantitative RT-PCR (qRT-PCR) was carried out in triplicate for each sample using 20 ng cDNA, TaqMan Universal PCR Master Mix (Applied BioSystems) and 1 µl of the specific TaqMan custom gene expression assay for the gene of interest (Applied Biosystems). To quantify gene expression, PCR was performed at 95ºC for 10 minutes, followed by 40 cycles at 95ºC for 15 seconds, 60ºC for 30 seconds and 72ºC for 30 seconds using an ABI Prism 7700 Sequence Detection System. As an internal control for the amount of template cDNA used, gene expression was normalized to the mouse β-actin gene using the Mouse β-actin Endogenous Control (VIC/MGB Probe, Primer Limited). Relative expression was calculated as $RQ=2^{-\Delta\Delta Ct}$.

Protein extract preparation

Tissues were immediately frozen in liquid nitrogen after extraction and homogenized in a 20 mM Tris buffer pH 7.4, containing 150 mM NaCl, 1% Triton X-100, 10 mM EDTA and Complete® protease inhibitor cocktail (Roche Applied Science). Then, tissue extracts were centrifuged at 12.000 rpm at 4ºC and supernatants were collected. Protein concentration was quantified by the bicinchoninic acid technique (BCA protein assay kit, Pierce Biotechnology, 23225). For protein extracts derived from cultured cells, cells were washed with cold PBS and lysed in a buffer containing 1% NP-40, 20 mM HEPES (pH 7.9), 10 mM KCl, 1 mM EDTA, 10% glycerol, 1 mM orthovanadate, 1 mM phenylmethanesulfonyl fluoride (PMSF), 1 mM dithiothreitol, 10 µg/ml aprotinin, 10 µg/ ml leupeptin and 10 µg/ml pepstatin. Lysates were centrifuged at 12.000 rpm at 4ºC and supernatants were collected. Protein concentration was quantified by the bicinchoninic acid technique (BCA protein assay kit, Pierce Biotechnology, 23225).

Immunoblotting

A total of 25 µg of protein sample was loaded on either 8% or 13% SDS-polyacrylamide gels. After electrophoresis, gels were electrotransferred onto polyvinylidene difluoride (PVDF) membranes (Millipore). Then, membranes were blocked with 5% non-fat dried milk in PBT (phosphate-buffered saline with 0.05% Tween 20) and incubated overnight at 4°C with primary antibodies diluted in 3% non-fat

dried milk in PBT. After three washes with PBT, membranes were incubated with the corresponding secondary antibody at 1:10.000 dilution in 1.5% milk in PBT and developed with Immobilon Western Chemiluminescent HRP substrate (Millipore, P36599A) by using Odyssey® Fc Imaging System (LI-COR, Lincoln, NE, USA). Unless otherwise specified, immunoblotting against ß-actin was used as sample processing control (LOAD) for the immunoblots shown in this article.

GFP-LC3 degradation assay by flow cytometry

Primary MEFs at 80% confluency from stably expressing GFP-LC3B WT and ATG4A-only mice were incubated in Dulbecco's modified Eagle's medium (DMEM, Sigma-Aldrich) complemented with heat-inactivated fetal bovine serum as control condition, in amino acid-free Earle's balanced salt solution (EBSS, Sigma-Aldrich) to induce autophagy and in EBSS with Bafilomycin A1 (50 nM, Enzo Life Science) to block the autophagy flux. After 4 hours of incubation, cells were trypsinized, pelleted by centrifugation, washed with Dulbecco's Phosphate Buffered Saline (DPBS), and pelleted again. Cell pellets were resuspended in DPBS supplemented with 5% of heat-inactivated FBS to a density of 10^5 cells/mL, kept in ice and GFP fluorescence intensity was immediately analysed by Fluorescence-Activated Cell Sorter (BD FACSAria Il, BD Biosciences). Data analysis and graphical representation were done using the free software Flowing Software 2.5.1. The level of the GFP fluorescence intensity was normalized to the level of the control sample, set at 100%.

Automated fluorescence microscopy

MEFs stably expressing fluorescent markers were seeded in 96-well imaging plates (BD Falcon, Sparks, USA) 24 hours before stimulation. Cells were treated with the indicated agents for 4 hours. Subsequently, cells were fixed with 4% PFA and counterstained with 10 µM Hoechst 33342. Images were acquired using a BD pathway 435 automated microscope (BD Imaging Systems, San Jose, USA) equipped with a 40X objective (Olympus, Center Valley, USA). Images were analyzed for the presence of fluorescent puncta in the cytoplasm using the BD Attovision software (BD Imaging Systems). Cell surfaces were segmented and divided into cytoplasmic and nuclear regions according to standard proceedings. RB 2x2 and Marr-Hildreth algorithms were used to detect cytoplasmic GFP-LC3 positive dots.

Long-lived protein degradation (LLPD)

LLPD was assessed as described previously (22). Briefly, MEFs were seeded in 24-well plates in 0.5 ml RPMI 1640/10% FBS (complete medium; "CM") containing 0.1 µCi/ml 14C-labeled L-valine (Vitrax, VC 308), and labelled for 3 days in a humidified incubator at 37 °C and 5% CO2. Next, cells were washed once with 0.5 ml CM supplemented with 10 mM cold (nonradioactive) L-valine (Sigma, V0513) ("CM-V"), and incubated in 0.5 ml CM-V for 18 h ("the chase period"). Subsequently, the cells were washed once with 0.5 ml CM-V or EBSS (Earle's balanced salt solution; Gibco, 24010043) amino acid starvation medium supplemented with 10 mM L-valine ("EBSS-V"), and thereafter incubated in either 0.25 ml CM-V containing 0.1% DMSO or 0.25 ml

EBSS-V containing 0.1% DMSO or 100 nM bafilomycin A1 (BafA1; Enzo) for 4 h ("the LLPD sampling period"). Cellular proteins were precipitated by placing the plates on ice for 2 min and adding 50 µl ice-cold PBS/2% BSA and 200 µl ice-cold 25% trichloroacetic acid (TCA) to each well. After overnight shaking at 4 °C, the solutions from each well were transferred to tubes and centrifuged at 5 000 x g for 10 min at 4 °C. The supernatants (TCA-soluble fractions) were transferred to scintillation tubes with 5 ml Opti-Fluor scintillation liquid (PerkinElmer Life Sciences) and mixed by vortexing. The pellets and insoluble material left in the wells (together making up the TCA-insoluble fractions) were solubilized by adding 250 µl 0.2 M KOH to each and agitating on roller/shaker for 1 h at room temperature. The resulting solutions were merged and mixed with 5 ml Opti-Fluor scintillation liquid by vortexing. Radioactivity was measured with a liquid scintillation counter (Packard Tri-Carb 2100TR). LLPD rate was calculated as the percentage of radioactivity in the TCA-soluble fraction relative to the total radioactivity in the TCA-soluble and -insoluble fractions, divided by the LLPD sampling period incubation time. BafA1-sensitive LLPD (indicating lysosomal LLPD) was calculated by subtracting the LLPD rates measured in cells that had been incubated with EBSS-V containing 100 nM BafA1 from that measured in cells that had been incubated with EBSS-V containing 0.1% DMSO.

Immunofluorescence and histology analyses of mice tissue sections and cells

For immunofluorescence analyses with tissue cryo-sections, sections were pretreated for 30 minutes in 1% H_2O_2/PBS, followed by 1 hour in blocking solution and incubated overnight with primary antibodies. Peroxidase activity was developed with the Elite Vectastain kit (Vector Laboratories) using diaminobenzidine (Dako). Sections were coverslipped with PermaFluor Aqueous Mounting Medium (Thermo Scientific). Digital images were captured with a Nikon Eclipse 80i optical microscope using the software NIS-Elements Basic Research. For paraffin sections, slides were deparaffinized and rehydrated. Slides or wells were blocked in 10% goat serum for 10 minutes, incubated with primary antibodies overnight at 4ºC, washed in PBS, incubated for 40 minutes with secondary antibodies, thoroughly washed in PBS, and stained with DAPI for nuclear staining. For immunofluorescence analyses of MEFs, cells were grown on 96-well black clear tissue culture-treated plates, washed in PBS, and fixed in 4% paraformaldehyde in PBS at room temperature for 10 minutes. Primary antibody was diluted 1:100 in PBS and incubated overnight at 4ºC. Samples were washed 3 times in PBS for 15 minutes each. Secondary antibody was diluted 1:300 in PBS, and incubated at RT for 1 hour. Samples were washed 3 times in PBS for 15 minutes each and analyzed by fluorescence microscopy.

Light and fluorescence microscopy analyses

IHC samples were analysed in a Leica DM4 B Upright Microscope with a Leica DFC 7000 T camera. Images were processed with LAS X software (Leica Application Suite X software, Leica Microsystems). Fluorescence microscopy images were acquired on an Axio Observer Z1 platform with a Plan-Apochromat 40X/1.3, (working distance, 0,21 mm) equipped with an ApoTome.2 system and an Axiocam MRm camera

(from Carl Zeiss, Jena, Germany). Zeiss Immersol® immersion oil was used for all microscopic analyses. ImageJ (National Institutes of Health, NIH, v. 1.53e) was the software used for image analysis and quantification.

Proteinase K protection assay

Cells were seeded in 6-well plates and autophagy induction was done by exposure to EBSS medium for 4 hours. Induction was stopped by trypsinization, and cells were washed with DPBS 1X and ruptured in homogenization buffer (20 mM HEPES at pH 7.6, 220 mM mannitol, 70 mM sucrose and 1 mM EDTA pH 8) by giving 10 strokes with a 27-gauge needle and a syringe (performed in ice). Samples were centrifuged at 4ºC for 5 minutes at 500 x g and the supernatants were again centrifuged at 7700 x g. Each pellet was resuspended in homogenization buffer, in enough volume to subdivide samples into four tubes: control (samples just the homogenization buffer); with the addition of Triton X-100 until 0.5% final concentration; with the addition of proteinase K (Roche, Ref. 03115879001) up to a final concentration of 50 µg/ml; and with the addition of both, proteinase K and triton. Samples were incubated for 45-60 minutes at 55ºC and immediately after, precipitated with 1:1 v/v trichloroacetic acid (TCA) at 10% in ice for 30 minutes. Samples were centrifuged at 12000 x g at 4ºC for 5 minutes and then washed twice with ice-cold acetone. Pellets were resuspended in 30 µl of Laemmli sample buffer (described in WB section), boiled at 95ºC for 5 minutes, and directly loaded and analysed by western blotting.

Protein aggregation assay

Cells stably-expressing RFP-p62 were seeded in 96-well plates with DMEM medium. Puromycin was added to the medium at 10 mg/ml (final concentration) in 20 mM HEPES buffer (pH 6.2 – 6.8) for 24 hours, to induce protein aggregates across the cytoplasm. Samples were fixed after 9 and 20 hours of exposure to measure aggregate formation, the number of cells with aggregates, and cell viability. As a complementary experiment, autophagy induction was performed in 96-well plates. At 0, 9, and 20 hours of exposure, the medium was changed to an EBSS medium to induce autophagy. Wells with DMEM+puromycin were used as controls at the corresponding time intervals. After 2 hours of autophagy induction, cells were fixed as previously described to quantify the decrease in the number of protein aggregates.

Blood and plasma parameters.

Animals were starved for 6 hours before measurement to avoid any possible alteration in blood glucose concentrations as a result of food intake. Blood was extracted directly from the mandibular sinus after anesthetizing mice with isoflurane. In the case that mice were previously euthanized, blood was obtained by cardiac puncture. Determination of hematological parameters was performed with the Abacus Junior hematology analyzer (Diatron Kft). Levels of serum insulin, growth hormone, leptin and adiponectin were measured with ELISA kits following the manufacturers' protocols (Merk Millipore, Rat/ Mouse ELISA kits, Ref. insulin EZRMI-13K; Ref. growth hormone EZRMGH-45K, Ref. leptin EZML- 82K; Ref. adiponectin EZMADP- 60K).

Levels of plasma IGF-1 were measured with Quantikine® ELISA kit following its corresponding protocol (R&D systems, Ref. MG100, SMG100, PMG100). Mice blood samples were collected in the presence of EDTA. Samples were then centrifugated at 3000x g at 4ºC for 15 minutes. Plasma samples were collected in Eppendorf tubes and stored at -80ºC until further analysis. Samples aimed to measure adiponectin and IGF-1 needed to be diluted (1:1000 v/v and 1:500 v/v, respectively) before the analysis (buffers were provided in the kits). Samples were analysed by duplicate in 96-well plates, where standard preparations for the calibration curves, quality controls, and blanks were also loaded. Absorbance was read at 450 and 590 nm in a multi-mode microplate reader (Synergy HT, Biotek) and the differences in the lectures were recorded for further data processing. Dose-response curves were fitted to a 5-parameter logistic equation, and calculations were performed with GraphPad Prism 9 software.

Senescence-associated beta-galactosidase staining.

Whole tissue samples were washed in PBS (pH5.5) before being fixed in 0.5% glutaraldehyde overnight and washed 2 × 15 min in PBS (pH5.5) at 4°C. SA-β-gal activity was assessed after incubation in X-Gal solution for 90 min at 37°C.

Analysis of bone structure

All tibia samples were scanned by high-resolution micro-computed tomography (SkyScan 1174, SkyScan, Kontich, Belgium). The small sample-holder device for µCT was used to fit the specimen with the long axis perpendicular to the floor of the specimen holder and the x-ray source. Images were obtained by 50 kV X-ray tube voltage and 800 µA. All specimens were scanned using a 0.5 mm aluminium filter and at 9.6 µm pixel size resolution. For each specimen, a series of 613 projection images were obtained with a rotation step of 0.3° and frame averaging 2 for a total 180° rotation. The scanning time for each sample was approximately 2 hours using an exposure time of 5500 ms. Flat field correction was performed at the beginning of each scan. The images obtained during scanning were reconstructed using the software NRecon (SkyScan). The correction values of attenuation coefficient, beam hardering, smoothing and ring-artifact reduction were the same in all samples. For morphometric analysis in 2D and 3D, the software provided by the manufacturer (CTAn) was used. Region of interest (ROI) was manually delimited in each of the samples. For the analysis of the diaphyseal cortical region, 100 slices were chosen. Global grayscale threshold levels for this area were between 88 and 250. For the trabecular region, a total of 150 slices were selected and adaptative grayscale threshold levels between 63 and 250 were used. The morphometric parameters examined were bone mineral density (BMD), ratio of bone volume/ tissue volume (BV/TV), trabecular thickness (Tb.Th), trabecular number (Tb.N) and trabecular separation (Tb.Sp) for the trabecular area and connectivity density among trabeculae. The parameters were measured according to the ASBMR histomorphometry nomenclature (23).

In vivo analysis of motor functions

All *in vivo* analyses were performed with male or female mice aged 2 months. For all analyses, evaluators were unaware of mice genotypes until analyses were completed. At least 6 mice were used for each experimental group in this type of analysis.

Footprint analyses

Hindlimbs were dipped into red non-toxic paint, whereas forelimbs were blue painted. Mice were allowed to walk through a plexiglass tunnel where the floor of which was covered with a sheet of white paper (20×50 cm). The stride length for each mouse was analyzed.

Tail suspension test

Mice were suspended by their tails and evaluated after limb positions were stabilized (normally within 60 seconds). Positions were photographically captured laterally to measure the angle of the upper forelimb against the body axis.

Raised-beam test

Mice were acclimated to crossing a 100-cm-long wooden square beam (8-mm width) elevated 30 cm above a padded base. Mice were placed on the start platform and allowed to traverse the beam to the opposite end. The time needed to cross the entire length of the beam was measured and the number of paw slips was counted. One (1) point was awarded to each paw slip. Two (2) points were awarded to each mouse fall while the test was developed. Animals were videotaped while traversing the wooden square beam for a total of three trials. A blinded observer viewed videotapes and analyzed the data.

Rotarod test

An accelerating rotarod LE8500 (LSI, LETICA) was used to evaluate the neuronal response of mice. 6 mice for each genotype were subjected to 6 rod trials. The rod accelerated from 4 to 40 rpm in 5 minutes and remained at maximum speed for the next 5 minutes. Animals were scored for their latency to fall (in seconds) for each trial and rested a minimum of 10 minutes between trials to avoid exhaustion and fatigue.

Metabolic measurements

Metabolic parameters such as VO2, VCO2 and energy expenditure were obtained using the comprehensive lab animal monitoring system (Oxymax CLAMS, Columbus Instruments, Columbus, OH, USA) and analyzed following the manufacturer's instructions. Mice were monitored for the specific period of time indicated in each case and the first 24 h were discarded in the analysis, considering them as acclimation period.

Quantification and statistical analysis

All data acquisition and analyses were performed by investigators blinded to the experimental group. For biochemical analyses, a minimum of three samples per genotype were used for each analysis, while in vivo analyses included at least six mice per genotype, unless otherwise specified. These sample sizes are sufficient to determine

whether there is a biologically meaningful difference between different genotypes, given the known mouse-to-mouse variation in autophagy assessments in previous studies published over the past decade. As for in vitro studies, a sufficiently large number of cells/areas were analyzed to ensure the description of biologically meaningful differences, also following the methods from studies cited throughout the paper. Quantifications for fluorescence microscopy/IHC were performed by analyzing at least 50 cells per condition/mouse and the measurements were performed at least in 3 different mice per genotype/condition or in three replicas for the same condition unless otherwise specified. Moreover, results obtained in cells were reliably reproduced in at least three independent experiments. All experimental data are reported as mean ± SEM unless otherwise mentioned. The data from the analyses met the assumptions of the tests and the variance was similar between the experimental groups. Unpaired two-tailed Student´s t-test was used when comparing two experimental groups. The Prism program version 7.0 (Graph-Pad Software Inc.) was used for calculations and P values lower than 0.05 were considered significant.

RNA-Seq

RNA extracted from mice liver samples of WT and ATG4A-only mice was processed by the company Novogene to prepare an unstranded mRNA library (poly-A enriched) and later sequenced using the NovaSeq X Plus platform. 6 Gb per sample were sequenced, generating 150 bp paired-end reads. The resulting FASTQ reads were trimmed of the Illumina library adapters using *cutadapt* and transcript quantification was carried out using Salmon v.1.10.3 and mouse GENCODE GRCm39 vM32 as transcriptomic reference. Quantification data was summarized to gene level and imported into R using the *tximeta* package, and afterwards, differential expression analysis was conducted using DESeq2. To study ATG4A-only vs. WT transcriptomic changes, samples were tested using the likelihood ratio test (LRT), comparing the full model — genotype + sex + age (previously scaled)— versus a reduced model, which only accounted for sex and age. The subsequent analysis was performed using the Benjamini-Hochberg p-adjusted value result of the LRT test, and the $\log_2$FC of ATG4A-only vs. WT expression. For the GSEA analysis, a "rank" variable was calculated as $-\log_{10}$(p-value) * sign($\log_2$FoldChange), and this gene ranking was used to compare ATG4A-only transcriptional profile to different signatures using the *fgsea* R package. Firstly, the Hallmarks subset of the Mouse Molecular Signatures database (MSigDB) (version 2023.2) was used to find alterations in well-defined biological processes. In addition, a collection of gene expression data from microarrays and transcriptome sequencing was used to compare expression profiles of different progeria models against ATG4A-only expression profile: DNA repair-deficient progeroid model *Ercc*$^{/\Delta 7}$ (24); HGPS mouse model *Lmna*$^{G609G/G609G}$ (25), Cockaine Syndrome mouse model *Csb*$^{m/m}$ *Xpa*$^{-/-}$ (26) and short-lived mouse model *RagC*$^{S74N/+}$ (27). Finally, senescence signatures described in multiple references (27-29) were also compared against ATG4A-only transcriptional profile.

RESULTS

Generation of *atg4b*$^{-/-}$*atg4c*$^{-/-}$*atg4d*$^{-/-}$ mice (ATG4A-only).

atg4b$^{-/-}$*atg4c*$^{-/-}$*atg4d*$^{-/-}$ mice (ATG4A-only) were generated by crossing murine models deficient for these genes. As previously reported, a*tg4b*$^{-/-}$ mice harbor an insertion of the cassette pT1betageo into the first intron of *Atg4B* gene, which results in absence of its transcript (Fig. 1A). *Atg4C* gene targeting was performed through a homologous recombination strategy allowing the replacement of exons 1, 2, 3 and 4 of the endogenous gene with a neo cassette (Fig. 1A). As for *Atg4D*, knockout mice were generated through the insertion of a PGK-Neo cassette into the first exon at its genomic locus (Fig. 1A). PCR analysis verified the homozygosity for all the mutations in ATG4A-only mice (Fig. 1B) and the absence of *Atg4B*, *Atg4C* and *Atg4D* transcripts was demonstrated by Real-time PCR (Fig. 1C). Interestingly, we found a significant upregulation of *Atg4A* gene expression in ATG4A-only cells, which could represent an attempt to compensate the loss of other ATG4 family members (Fig. 1C). Indeed, ATG4A-only mice showed increased tissue levels of ATG4A protease, as compared to WTs (Fig. 1D). Despite ATG4B, ATG4C and ATG4D deficiency, ATG4A-only mice had normal embryonic development and were born at Mendelian ratio. Moreover, ATG4A-only neonates were indistinguishable from their WT littermates (Fig. 1E) and their survival was equivalent. This evidence suggests that in the absence of the other three members of the ATG4 family, the activity of ATG4A protease alone is sufficient for the induction of the requested levels of autophagy which are essential for the viability of neonate mice, as reported for most autophagy-deficient models that result in embryonic or perinatal lethality (1). However, despite their normal embryonic and neonatal development, ATG4A-only mice soon developed several phenotypical manifestations, such as reduced size (Fig. 1E), which will be further addressed later in this manuscript.

Impact of simultaneous deletion of ATGB, ATG4C and ATG4D in autophagic degradation

To evaluate in detail the effects of simultaneous ATG4B, ATG4C and ATG4D deficiency in the context of autophagy, we decided to first generate mouse embryonic fibroblasts (MEFs) from triple knockout and WT embryos. Next, we performed autophagic flux experiments by subjecting WT and ATG4A-only cells to nutrient deprivation including conditions in which Bafilomycin A1 (BafA1), an inhibitor of lysosomal acidification and autophagosome–lysosomal fusion, was added to the culture medium. When lipidation of mATG8 proteins was analyzed in these experimental settings, we could observe that, as previously described, WT cells showed increased levels of lipidated mATG8 forms upon BafA1 treatment both in control and nutrient-free conditions (Fig. 2A). By contrast, ATG4A-only cells showed significant alterations in the status of all five murine ATG8s when compared to WT cells. Regarding LC3A and LC3B, ATG4A-only cells show an accumulation of the bands corresponding to either the uncleaved or unlipidated forms of these proteins (which cannot be distinguished by

immunoblotting in our experimental settings), together with a drastically reduced amount of the lipidated forms in all the conditions analyzed (Fig. 2A). In the case of GABARAPL1, ATG4A-only cells show a clear accumulation of its uncleaved form (which is absent in WT cells) together with reduced content of both the unlipidated and lipidated forms, as compared with WT cells (Fig. 2A). By contrast, ATG4A-only cells show slightly increased levels of GABARAP lipidated forms as compared to WT, whereas they show a clear accumulation of GABARAPL2 lipidated forms either in control or nutrient free conditions (Fig. 2A). In ATG4A-only cells, BafA1 treatment induced a minor increase in the lipidated forms of LC3s and GABARAPL1, either in control or nutrient-free conditions, whereas the amount of GABARAP-II remained constant, even in the absence of nutrients. This suggests that irrespectively of showing lower (LC3s/GABARAPL1) or higher (GABARAP) content of lipidated mATG8s forms, ATG4A-only cells show a drastically reduced, almost totally impaired, autophagic flux for these proteins (Fig. 2A). By contrast, BafA1 treatment induced a substantial accumulation of GABARAPL2 lipidated form, both in control conditions and upon starvation, which was much higher to that observed in WT cells, suggesting an increase in the autophagic flux for this protein in ATG4A-only cells (Fig. 2A). At the subcellular level, ATG4A-only MEFs show a clear reduction in the number of dot-like structures positive for all LC3A, LC3B, GABARAP and GABARAPL1 both at control or starvation conditions, either in the presence or absence of BafA1 (Fig. 2B-C). By contrast, ATG4A-only cells show a higher number of GABARAPL2 positive structures than WT MEFs in all conditions analyzed (Fig. 2B-C), which is in line with our results from immunoblotting experiments. Altogether, these results suggest that ATG4A protease is able to proteolytically activate GABARAPL2 protein, but is only minimally able to do so for LC3s, GABARAP and GABARAPL1. To directly address this question, we transfected N- and C-terminal-tagged cDNAs of LC3 and GABARAP proteins into WT and ATG4A-only MEFs and analyzed the status of these proteins by immunoblot. As shown in Fig. 2D, we could detect bands corresponding to the uncleaved forms of LC3 and GABARAP proteins (pro-LC3s and pro-GABARAPs) in ATG4A-only cells, which derive from impaired activation of these substrates (Fig. 2D). As expected, accumulation of these bands was not detected in WT cells, with the exception of GABARAP, for which we could also detect residual unprocessed forms of the tagged protein in WT cells (Fig. 2D). Interestingly, GABARAPL2 is the only mATG8 efficiently primed ATG4A-only cells (although not as efficiently as in WT cells), which is in line with our previous immunblotting and immunofluorescence results (Fig. 2A-C). All these results show that the reduction of autophagic flux of ATG4A-only MEFs is caused by the inability of ATG4A to properly cleave the pro-forms of LC3A, LC3B, GABARAP and GABARAPL1. In this regard, ATG4A-only cells show accumulation of the autophagic substrates p62/SQSTM1, OPTN, NDP52 and NBR1 (Fig. 2A) and failed to efficiently clear both p62/SQSTM1 and ubiquitin-labelled proteins upon autophagy induction by starvation (Fig. 2E-F). Consistently, when GFP-p62/SQSTM was stably expressed in ATG4A-only MEFs, we observed that ATG4A-only cells showed fewer GFP-p62/SQSTM puncta than the corresponding WT control cells in each condition analyzed (Fig. 2G). Moreover, ATG4A-only MEFs failed to degrade GFP-p62/SQSTM upon

nutrient deprivation, contrary to WT cells, in which starvation-induced GFP-p62/SQSTM degradation was abolished by treatment with the autophagic flux inhibitor BafA1 (Fig. 2G). In line with these results, FACS-based quantification of GFP-LC3B degradation in ATG4A-only cells (30) confirmed an impairment in GFP-LC3B autophagic clearance in response to nutrient deprivation, contrary to the results in WT cells (Fig. 2H). Interestingly, when the fusion protein GFP-LC3B is stably expressed in ATG4A-only cells, a significantly reduced number of positive puncta for this reporter are detected in ATG4A-only cells in any of the conditions analyzed (Fig. 3A). Moreover, ATG4A-only cells tend to accumulate large protein aggregates containing GFP-LC3B, which are positive for endogenous p62/SQSTM and Ubiquitin (Fig. 3B). This is likely a consequence of substantially impaired GFP-LC3B priming by ATG4A, which might tend to aggregate when present in its pro-form as previously reported for other mATG8 proteins (31). In fact, proteinase K-based analyses, which allow detection of the presence of lipidated mATG8 proteins in both closed and unclosed autophagosomes revealed that a higher percentage of the lipidated LC3B of ATG4A-only cells is associated with proteinase K sensitive membranes, most likely immature unclosed autophagosomes (Fig. 3C). Thus, in order to quantitatively analyse the autophagic degradative activity of ATG4A-only cells, we next performed LDH sequestration assays, which specifically measure non-specific autophagic sequestration and degradation of the cytosolic enzyme lactate dehydrogenase (LDH) (32, 33). As shown in Fig. 3D, amino acid starvation-induced LDH sequestration was substantially reduced in ATG4A-only MEFs compared to WT cells, indicating a defect in autophagosome formation. In agreement, ATG4A-only MEFs showed significantly lower SAR405 (PI3KC3-inhibitor) and Bafilomycin A1 (lysosomal ATPase inhibitor)-sensitive degradation of long-lived proteins compared to WT MEFs (Fig. 3D). Of note, the stronger reduction in LDH sequestration in ATG4A-only cells compared to that observed in long-lived protein degradation may suggest a compensatory upregulation of non-autophagic proteolytic mechanisms.

These results show that ATG4A protease has limited activity towards mATG8 proteins in MEFs, being able to activate a residual fraction of them, which can be subsequently lipidated, except for GABARAPL2, which is efficiently primed by ATG4A. Thus, the sole presence of ATG4A leads to a severe (albeit not complete) defect in autophagic degradation, which occurs at a step prior to phagophore closure in cultured cells.

Recruitment of ATG proteins in ATG4A-only cells.

The autophagy process requires the coordination, assembly and interaction of a variety of protein complexes hierarchically involved in different steps of autophagy regulation, autophagosome formation and maturation (34). We thus generated specific cell lines stably expressing different fluorescent markers for a variety of proteins involved in different steps of autophagy regulation or execution and analysed their basal subcellular localization and starvation-induced recruitment in WT and ATG4A-only

MEFs. Autophagosome biogenesis is regulated by the combined activity of Vps34- and ULK1-containing complexes, which are recruited to autophagosome-forming sites during autophagy initiation (35). As shown in Fig. 3E-F, the number of subcellular structures positive for both WIPI-1 and DFCP-1, which are recruited to membrane domains enriched in PtdIns3P by Vps34 to participate in autophagosome biogenesis (36), was significantly increased in ATG4A-only cells. This is in line with previous reports showing an increased number of WIPI2 puncta in the absence of either ATG5 or ATG3 (34). Consistently, ATG4A-only cells also showed increased protein levels of ATG14L, a key player of the Vps34-containing complex, as measured by immunoblotting analyses (Fig. 3G). On the other hand, ATG4A-only MEFs show a reduced number of punctate structures positive for Atg13, indicative of the ULK1-complex, as compared to that observed in WT MEFs (Fig. 3E, F). Furthermore, cellular levels of ATG13, ATG101 and FIP200, all essential components of the ULK1-containing complex, are also reduced in ATG4A-only cells (Fig. 3G). Similarly, the abundance of ATG5-positive structures, indicative of nascent autophagosomes (37), was reduced in ATG4A-only MEFs upon starvation conditions (Fig. 3H), which points to defects in autophagosome formation. In line with these results, ATG4A-only cells showed a reduction in the number of syntaxin17 (STX17TM)-positive structures (Fig. 3E-F), which correspond to successfully-formed autophagosomes (38). STX17 is a soluble N-ethylmaleimide–sensitive factor attachment protein receptor (SNARE) involved in autophagosome-lysosome fusion through its interaction with the vesicle-associated membrane protein 8 (VAMP8) at the lysosomal/endolysosomal membrane (38). ATG4A-only MEFs also showed a reduced number of VAMP8-positive vesicles, either upon basal or starvation conditions (Fig. 3E-F). All the described autophagy defects of ATG4A-only cells not only reduced their autophagic degradative capacity but also decreased their ability to cope with protein aggregates. As previously mentioned, ATG4A-only MEFs accumulated Ubiquitin- and p62-positive protein aggregates upon GFP-LC3B overexpression (Fig. 3B). Consistently, they were highly susceptible to puromycin-induced protein aggregation. Puromycin is known to promote the formation of polyubiquitinated protein aggregates, which are then marked with p62 for its degradation by autophagy (Fig. 3I-J). In fact, ATG4A-only cells are more prone to form and accumulate puromycin-induced protein aggregates as compared with WT cells. Interestingly, starvation was able to reduce aggregate content in WT cells after 9 hours of exposure to puromycin, whereas it had no effect in ATG4A-only cells (Fig. 3J). Moreover, the accumulation of these aggregates negatively impacted cell survival, which is significantly reduced in knockout cells compared to WT after 20 hours of exposure to puromycin (Fig. 3J).

These results show that in cultured cells, the combined deficiency of ATGB, ATG4C and ATG4D leads to a situation in which reduced recruitment of ULK1-containing complexes is accompanied by accumulation of structures positives for both WIPI1 and DFCP1 and finally to a decrease in the rate of autophagosome formation, which is consistent with the observed reduction in autophagic degradation and renders cells more susceptible to stressors that require autophagic activity for cell survival, such as protein aggregate clearance.

ATG4A-only mice show tissue-specific autophagy alterations.

We have shown that the simultaneous loss of ATG4B, ATG4C and ATG4D proteases leads to severe impairment of autophagic degradation in cultured MEFs. Thus, we decided to evaluate the degree of autophagy proficiency in ATG4A-only mice by analyzing the status of autophagy-relevant proteins in tissues from these animals. We first performed immunoblotting analyses of mATG8 proteins in a variety of tissue extracts from 4-weeks-old *ad libitum*-fed WT and ATG4A-only animals, whose feeding cycle was synchronized before sacrifice, to ensure the reliability of autophagy-related analyses, as previously reported (39). As shown in Fig. 4A, the status of GABARAP, GABARAPL1 and GABARAPL2, in ATG4A-only mice tissue extracts is mostly similar to that observed in cultured MEFs, as revealed by immunoblotting experiments. ATG4A-only mice samples show an increased presence of GABARAP and GABARAPL2 lipidated forms. Regarding GABARAPL1, ATG4A-only mice samples show accumulation of uncleaved pro-GABARAPL1, as previously observed in MEFs immunoblotting analyses, although in some tissues, such as skeletal muscle or lung, lipidated GABARAPL1 was also observed (Fig. 4A). In the case of LC3 proteins, their lipidation status was tissue-dependent in ATG4A-only samples. In most of the tissues analysed, including heart, lung, kidney or liver, both LC3A and LC3B showed a similar status than in MEFs. As shown in Fig. 4A, we could detect an accumulation of pro-LC3s/LC3-I forms and a reduction in lipidated LC3s as compared to WT samples. However, in brain and skeletal muscle tissues, the amounts of lipidated forms of these proteins were more abundant in tissue extracts from ATG4A-only mice than in those from WT mice (Fig. 4A). Immunofluorescence analyses showed that the number of positive puncta for mATG8 proteins in ATG4A-only mice tissues was consistent with our immunoblotting results, except for GABARAPL1, for which we could detect an increased number of positive structures in all tissues analysed. The reason for this discrepancy is unclear, although it is possible that the excess of GABARAPL1 puncta in ATG4A-only mice tissues could correspond to protein aggregates of pro-GABARAPL1, which could accumulate in the combined absence of ATG4B/C/D. Additionally, some positive puncta for GABARAPL1 could represent unclosed pre-autophagosomal structures, in which this protein remains lipidated in the absence of ATG4D, which is the main delipidating enzyme for mATG8s in mammalian cells (11). Interestingly, the subcellular distribution of LC3 proteins in ATG4A-only mice cells was tissue-dependent, in line with our immunoblotting results. In fact, we could observe an increase in the number of positive puncta for both LC3A and LC3B in skeletal muscle, whereas in liver, we detected a significantly lower number of LC3s puncta in ATG4A-only samples (Fig. 4B). Irrespectively of these differences in the status of LC3 proteins, we could observe a significant accumulation of the autophagic substrate p62/SQSTM1 in most ATG4A-only tissues (Fig. 4A, C). In fact, p62/SQSTM1 accumulation in skeletal muscle or in different regions of the SNC (analyzed either by immunoblotting or immunohistochemistry) was comparable to that observed in tissues in which LC3 proteins showed reduced lipidation, such as liver or heart, which suggests that the observed alterations in mATG8 proteins lead to defects in autophagy-mediated protein quality control in ATG4A-only mice tissues (Fig. 4A, C). These features were

also accompanied by both a reduction in the levels of essential components of the ULK1-containing complex, such as ULK1, FIP200, ATG13 or ATG101 and an increase in the levels of ATG14L, a key player of the Vps34-containing complex (Fig. 4D), which is in line with our results in cultured MEFs (Fig. 3G).

ATG4A-only mice show reduced lifespan and features of accelerated aging

The combined deficiency of ATG4B, ATG4C and ATG4D leads to defects in the processing of most mATG8 proteins and in the status of other components of the autophagic pathway, ultimately resulting in a reduction of autophagic degradation in ATG4A-only cultured cells and mice tissues. Moreover, as previously mentioned, the autophagy defects of ATG4A-only mice led to the development of a strong phenotype after the first weeks of life. After weaning, ATG4A-only mice showed reduced size and weight despite normal feeding habits (Fig. 5A, 1E), until they prematurely died, being their median survival of 133 days (although they showed high variability in their lifespan, which ranged from 26 to 387 days) (Fig. 5B). This reduction in ATG4A-only mice lifespan suggested the existence of major pathologies. ATG4A-only mice reproduced most of the phenotypical characteristics observed in mice deficient for either *Atg4B, Atg4C* or *Atg4D*. These features included symptoms of balance-related disorders, such as tilted head or circling behaviour, derived from deficient otoconial development (Fig. 5C and Supplementary Video 1), first observed in *atg4b*$^{-/-}$ mice (37). Triple mutant mice also showed strong signs of ataxia, including limb-clasping reflexes when they were suspended by their tails (Fig. 5D), abnormal gait (Fig. 5E), lower skeletal muscle strength, as confirmed by the grip test (Fig. 5F) and poor performance in both raised beam and rotarod tests (Fig. 5F-G). These ataxic features were similar but more extreme than those observed in aged *atg4d*$^{-/-}$ mice (11). Moreover, ATG4A-only mice showed haematological alterations that were more severe than those observed in *Atg4C*-deficient mice (12), as they presented thrombocytosis, reduced haematocrit, increased circulating granulocytes and decreased mature lymphoid populations (Figs. 5H-K). In addition to all these features, already present at some extent in *Atg4B-, Atg4C-* and *Atg4D-deficient* mice, triple mutant mice showed additional phenotypical manifestations. Anatomical analyses of 3-month-old ATG4A-only mice revealed alterations in the relative size of several organs, as compared to the corresponding age-matched WT controls. As shown in Fig. S1, ATG4A-only mice showed increased relative size of the heart, spleen, brain, pancreas and thymus and a reduction in the relative size of submaxillary glands and absence of white adipose tissue. Moreover, histological analyses also revealed a series of structural alterations in many organs (Fig. 6A). In fact, the skin of triple mutant mice showed signs of atrophy, with areas of hyperkeratosis, some cystic dilatations and a clear reduction of the subcutaneous fat compared with their WT littermates. Similarly, the amount of scapular brown fat was also reduced. ATG4A-only mice kidneys showed abnormally reduced size and thickness of the cortical area, with cystic dilatation of the tubules in several individuals and major areas of renal fibrosis. Significant fibrotic areas also appeared in the lungs of ATG4A-only mice and the pancreas presented smaller islets

and areas of autolysis in some individuals were observed. ATG4A-only splenic tissue showed signs of white pulp depletion, lymphoid depletion and myelopoiesis, whereas the external wall of the colon appeared to be thickened, indicating moderate hypertrophy of the muscularis externa in knockout mice. Finally, the hearts of ATG4A-only mice were hypertrophic in relation to body weight and showed large fibrotic areas in some individuals. Moreover, μCT analysis of tibias revealed ATG4A-only mice suffer from premature bone loss involving a reduction in total bone volume, trabecular number and a reduction in bone mineral density (BMD) (Fig. 6B). Analysis of biochemically-relevant serum parameters revealed normal levels of sodium, phosphorus, creatinine, creatine kinase, albumin, globulins, lipase or bilirubin. By contrast, we noticed a significant increase in alanine aminotransferase levels (characteristic of liver damage) and a decrease in alpha-amylase, triglycerides, cholesterol and bile acids in ATG4A-only mice as compared to age-matched WT mice (Fig. 6C). Taken together, all these phenotypic alterations demonstrate the critical relevance for autophagy in tissue homeostasis and functionality. Due to the profound implications of autophagy in cell and tissue homeostasis, it is not surprising that the systemic severe reduction of autophagic activity in ATG4A-only mice simultaneously impacts the functions of multiple tissues, which ultimately may lead to premature death. However, we could not detect any drastic damage which may justify ATG4A-only premature death by itself. Instead, it seems to be a consequence of the cumulative alterations and synergistic detrimental effects. It is interesting that many of the alterations found in ATG4A-only mice at a young age, such as loss of muscle strength, skin atrophy, loss of subcutaneous fat, lung and kidney fibrosis, cardiac hypertrophy, lymphoid depletion or reduced BMD, are found in aged individuals and are also characteristic of progeroid murine models with accelerated aging (40). In this sense, one characteristic of progeroid mice is metabolic reprogramming, which involves alterations in the expression and activity of important metabolic gene regulators or deregulation of somatotroph signalling, among other features (25, 26, 41, 42). Thus, we analyzed several metabolic and hormonal parameters whose alteration is common to different progeroid mice models. As shown in Fig. 6D, ATG4A-only mice showed reduced circulating levels of de adipokine leptin, which is consistent with their absence of WAT. Conversely, ATG4A-only mice show higher circulating adiponectin levels (Fig. 6D), as compared to their WT littermates. Interestingly, the simultaneous occurrence of lipodystrophy, reduced plasma leptin and high circulating adiponectin has been found in several murine models of premature aging (25, 43). ATG4A-only mice also manifest deregulation in the somatotroph axis which is similar to that observed in progeroid mice (25, 26, 44). Specifically, plasma GH concentration is abnormally elevated in ATG4A-only mice, whereas circulating IGF-I levels are normal or even reduced, likely as a consequence of liver growth hormone resistance, as previously reported (41) (Fig. 6D). Moreover, ATG4A-only mice show additional phenotypic manifestations that are also found in different mice models of accelerated aging, such as increased hepatic glycogen deposits (26, 43) or increased respiration rates, measured by O_2 consumption and CO_2 production, which are decreased in old mice but increased in progeroid animals (45-47) (Figs. 6E-F).

ATG4A-only mice share transcriptomic signatures with progeroid mice and show increased senescence

Prompted by our previous results, we decided to evaluate if the observed aging-like phenotype of ATG4A-only mice could be associated with alterations at the transcriptomic level. Thus, we conducted bulk RNA sequencing (RNA-seq) from livers of ~3-month-old WT and ATG4A-only mice. Principal-component analysis (PCA) clustered samples by genotype (Fig. S2), with 401 genes differentially expressed in ATG4A-only livers (241 upregulated and 160 downregulated), as compared to WT mice (Supplementary Table 1). In addition to the genes coding for ATG4B-C proteases, 17 members of the MUP (major urinary protein) family were among the most significantly downregulated genes (Fig. 7A C, D and Supplementary Table 1), suggesting that the expression of the MUP cluster is downregulated in both males and females. Reduction of the expression of MUPs in the liver was validated by immunoblotting (Fig. 7D). Interestingly, MUP expression is highly dependent on somatotroph axis signalling (48) and a reduction in their expression has been observed both in old senescent mice (49) and in progeroid animals. Serpinb1a, which reduces IFN-dependent inflammatory responses through IKBKE degradation (50) or DIO1, an iodothyronine deiodinase involved in thyroid hormone metabolism, whose activity is decreased in conditions of liver damage and mice suffering from accelerated aging (51), were also among the most significantly downregulated genes in ATG4A-only mice livers (Fig. 7A, C-D and Supplementary Table 1). Among the significantly upregulated DEGs, we could find several genes coding for pro-inflammatory cytokines from the CC and CXC chemokine families, as well those coding for Grandzymes A, B as well as proinflammatory Calgranulin B (S100a9), whose overexpression was confirmed by immunoblotting (Fig. 7D). This is interesting, as hepatocyte-specific S100a8 and S100a9 transgene expression in mice has been shown to cause hepatocyte Cxcl1 induction and systemic neutrophil enrichment (52). Consistently, we also found overexpression of the cytokine Lipocalin-2 (LCN2) in mutant mice livers, which was also confirmed by immunoblotting (Fig. 7D). Interestingly, LCN2 is able to regulate LC3 lipidation through interaction with ATG4B (53) and its expression in liver is markedly increased upon liver injury in a process mediated by pro-inflammatory cytokines (54). In line with these observations, pathway enrichment analysis showed that ATG4A-only mice livers presented significant upregulation of several inflammatory signatures, such as interferon γ (IFNγ) and IFNα responses, tumor necrosis factor (TNFα) signalling and interleukin-6 (IL-6) signalling (Fig. 7B and S3, S5A). Moreover, we also found upregulation of allograft rejection (which involves enrichment in pro-inflammatory genes and cytokines among others), complement signalling and UV response signatures in ATG4A-only mice livers (Fig. 7B and S3, S5A), whereas most significantly downregulated signatures were fatty acid synthesis and peroxisome and bile acid metabolism signatures, which are consistent with the observed lipodystrophy and low circulating bile acids of mutant mice (Fig 7B and S4, S5B).

The high expression of inflammatory signatures in the liver, together with the observed increase in circulating granulocytes in ATG4A-only mice strongly suggest an increase in 'inflammaging', a chronic process characteristic of aging which involves a

systemic state of myeloid inflammation. These results reinforce the idea that the systemic reduction of the autophagic potential of ATG4A-only mice leads to the development of aging-associated pathologies at a young age. Accordingly, comparison of ATG4A-only mice DEGs with datasets from different progeroid mice, including Cockayne syndrome (26), Hutchinson-Gilford progeria (25), XPF progeria (44) or *RagC*$^{S74N/+}$ mice, recently described as a new mice model of accelerated aging (27), yielded a striking enrichment of upregulated and downregulated genes (Fig 7B, E, S6A). In this sense, although the exact molecular causes of progeroid syndromes are diverse and specific for each of them, the vast majority are caused by defects either in the maintenance of the nuclear envelope or in DNA repair mechanisms and are characterized by hyperactivation of DNA damage responses (DDR) (55). The activation of DDRs, which may lead to cell cycle arrest, senescence or apoptosis, is mainly regulated by p53 and/or p16-depending pathways (56). Interestingly, when we analyzed markers of DNA damage, such as H2AX, and the status of the main DDR effectors, such as p16 or p53, we observed a clear increase in the levels of these proteins and their phosphorylated forms in ATG4A-only mice tissues, as compared with age-matched WT littermates (Fig. 8A). Consistently, immunohistochemistry analyses revealed nuclear accumulation of p21 in ATG4A-only mice livers (Fig. 8B) and whole mount senescence-associated beta-galactosidase staining from 4-month ATG4A-only mice livers revealed a marked increase in comparison with age-matched control mice (Fig. 8B). These results show an hyperactivation of DDR in ATG4A-only mice, which likely drives the observed upregulation in the expression of inflammatory genes and increased senescence. In line with these results, when we compared the differentially expressed genes (DEGs) from our RNA-Seq experiments with datasets from mice models of senescence inflammatory responses (SIR) (28) or senescence-associated secretory phenotype (SASP) (29), we found a significant enrichment of upregulated DEGs from ATG4A-only mice livers among those overexpressed in those datasets (Fig. 8C, S6B), reinforcing the idea of a pro-inflammatory, pro-senescent state in ATG4A-only mice.

Collectively, all these results show that the reduction of autophagic competency caused by the simultaneous loss of ATG4B, ATG4C and ATG4D proteases in mice leads to a progressive loss of organismal fitness, premature multimorbidity and drastically shortened lifespan, with molecular, histological, metabolic and transcriptomic alterations which are common to aged individuals and are characteristic of murine models of human premature aging syndromes.

DISCUSSION

In this work, we have progressed in the characterization of the roles of ATG4 proteases and autophagy through the generation and characterization of a new murine model (ATG4A-only mice), simultaneously deficient for *Atg4B, Atg4C* and *Atg4D.* Despite the efforts to establish the specificity of ATG4 proteases for the processing and delipidation of LC3/GABARAP proteins in mammalian cells, the precise *in vivo* roles for each of the ATG4 proteases towards their physiological substrates, mATG8 proteins, has remained elusive for the most part, with some studies showing contradictory results (57-59). Among other factors, this is due to the degree of functional redundancy in ATG4 family and the lack of appropriate cellular and animal models. In this sense, the generation of these ATG4A-only mice represents a unique opportunity not only to understand the specific functions of ATG4A protease *in vivo*, as it is the only functional ATG4 member in these mice, but also to get new insights into the role of autophagy in mammalian physiology.

Our results indicate that among all pro-mATG8 proteins, ATG4A only efficiently processes pro-GABARAPL2. This effect was already observed, although at a lower extent in ATG4B-deficient cells and suggests that some kind of compensatory mechanism involving increased recruitment of GABARAPL2 to autophagic structures is operating. In fact, ATG4A-only cells and tissues show increased levels of lipidated GABARAPL2 in all the experimental conditions that we have tested (Fig. 2A, C and 4A-B). By contrast, ATG4A shows a limited priming activity against GABARAP and a drastically reduced (although not totally impaired) ability to activate the rest of pro-mATG8s. These results contrast with previous reports in which ATG4A has been shown to efficiently cleave GABARAP and GABARAPL1 proteins in cultured human cancer cells (57). The fact that these results were obtained in different experimental settings, involving both Parkin1 and ATG4A overexpression might account for the observed differences. Despite their deficiency in the processing of pro-LC3s, pro-GABARAP and pro-GABARAPL1, ATG4A-only cells and tissues show the presence of their lipidated forms, with an increased number of subcellular puncta positive for GABARAP proteins in most mice tissues. Although there might be other possible explanations for this apparent contradiction, the fact that ATG4A-only cells lack ATG4D, which is the main delipidating enzyme for mATG8s (18) and also ATG4C, which contributes to mATG8s delipidation in the absence of ATG4D (12), likely causes that the small fraction of GABARAP and GABARAPL1 primed by ATG4A (and subsequently lipidated) remains conjugated to membranes, as previously proposed (60). This is supported by the fact that GABARAP-II and GABARAPL1-II levels in ATG4A-only cells are higher than those observed in ATG4B KO cells, but similar to those observed in ATG4B/D double mutants (Fig. S7). In this regard, it is remarkable that the amount of LC3A and LC3B subcellular puncta and lipidated forms is tissue-dependent. In fact, most ATG4A-only tissues show reduced content of lipidated LC3s/LC3s puncta, except for skeletal muscle and liver, which show the opposite effect (Fig. 4A, B). The reason for this discrepancy is unknown, although it is not related to ATG4A levels, as its expression is not particularly high in these tissues (12). Other aspects, such as the existence of tissue-specific factors involved

in autophagosome formation/maturation or tissue-specific differences in the basal rate of autophagosome biogenesis, transport or degradation could contribute to explaining this observation.

In any case, the observed defect in mATG8s priming, together with the absence of ATG4B/C/D, which has been proposed to play a direct role in autophagosome formation (57), leads to the accumulation of unclosed pre-autophagosomal structures in ATG4A-only cells. This leads to a drastic reduction in the number of fully formed autophagosomes, as evidenced by the observed decrease in STX17-labelled puncta in ATG4A-only cells (Fig. 3E-F). In this scenario, autophagic flux and autophagy-dependent degradation are severely diminished, although not totally abolished. This indicates that the activity of ATG4A is sufficient to sustain the formation of a reduced number of functional autophagosomes, which in turn are likely able to support a minimal level of autophagy. However, this is not enough to prevent the accumulation of protein aggregates containing p62/SQSTM, which appear both in cultured cells upon proteotoxic stress and in mice tissues spontaneously (Fig. 3B, I-J). In this regard, it is interesting that ATG4A-only cells show a reduction in the recruitment of ULK1 protein complex to autophagic isolation membranes upon nutrient deprivation (Fig. 3E-F), which is consistent with the lower cellular and tissue content of ULK1, FIP200, ATG13 and ATG101 proteins (Fig. 3G, 4D), all components of this autophagy-initiating complex (35). This could be explained by the fact that lipidated forms of ATG8s play an important role in the recruitment of ULK1 complex to pre-autophagosomal membranes, being also required to promote ULK1-mediated phosphorylation of Vps34 complex components (61). In fact, the interaction between ULK1, FIP200, ATG13 and mATG8s stabilizes their association with the forming phagophore and the loss of mATG8s leads to reduced cellular levels of ULK1, FIP200 and ATG13 proteins in HeLa cells (61). Conversely, ATG4A-only cells show an increased presence of DFCP1 and WIPI1 positive structures, which although in apparent contradiction with the reduced accumulation of ATG13-containing puncta, is in agreement with previous studies reporting a similar accumulation of WIPI2 and DFCP1 puncta in both ATG5 and ATG3 KO MEFs, which might point to the existence of a feedback mechanism linking autophagic degradation and Vps34 complex activity

Irrespectively of these mechanistic considerations, which will be further addressed in future studies, the analysis of ATG4A-only mice has enabled us not only to precisely define the roles of ATG4A towards its physiological substrates, but also to understand how the degree of autophagy competency impacts longevity through the maintenance of proper tissue homeostasis and organismal fitness. It is important to consider that due to the essential functions of autophagy, murine models in which autophagic activity is totally abolished show either embryonic or perinatal lethality. This characteristic has largely precluded the study of the effects of reduced systemic autophagy in longevity, as the available mice models, such as Ambra-1 or Beclin-1 heterozygous mice show a relatively mild systemic autophagy reduction (62). Thus, the generation of ATG4A-only mice has allowed us to analyze the impact of a profound systemic autophagic impairment at a cellular, tissue and organism level. This is a relevant question, as it is known that

autophagic potential gradually declines as the organism ages and some environmental factors, including pollutants or nanoparticles, interfere with components of the pathway, reducing autophagic competency in a progressive way. ATG4A-only mice show a drastically reduced lifespan, prematurely showing features characteristic of aged mice, such as poor motor function, osteoporosis, tissue fibrosis, lymphopenia or an increase in inflammaging. Moreover, these autophagy-deficient mice manifest alterations which are specific to progeroid mice models, such as lipodystrophy with increased adiponectin levels, increased oxygen consumption, somatotroph axis de-regulation with increased GH, hepatic glycogen accumulation, increased DNA damage (manifested by hyperphosphorylation of H2AX) or hyperactivation of pro-senescent regulators such as p53, p16 or p21 with enrichment of pro-senescent transcriptional signatures at an early age. This evidence, together with the fact that ATG4A-only mice transcriptome shows enrichment of upregulated DEGs from several different progeroid models, establish a direct link between the level of systemic autophagy proficiency and the advance of aging in mammals. In fact, it is compelling that ATG4B-deficient mice, which present a limited although significant reduction in autophagy competency, only show a 7.25% and 5.3% reduction in their median and maximal lifespan respectively, whereas mice double deficient for ATG4B/C and ATG4B/D proteases show a more clearly reduced longevity, although not as short as that of ATG4A-only mice (Fig. 9D-F). This observation strongly supports the idea that despite the complexity of autophagy's roles, which can be highly diverse and cell- or tissue-specific, as well as the intricate molecular mechanisms involved in the regulation and execution of autophagy and related processes, the degree of autophagic competency ultimately emerges as a critical determinant of organismal longevity. Consequently, the specific upregulation of autophagy may represent a promising therapeutical strategy for addressing human accelerated ageing syndromes.

ACKNOWLEDGEMENTS

This work was supported by grants from Ministerio Ciencia e Innovación (Spain) (PID2021-127534OB-I00). We thank Drs. Alejandro Piñeiro Ugalde and Pedro Moral Quirós for helpful comments.

AUTHOR CONTRIBUTIONS

G. G-M-G., M. F. S., I. T-G., Á.F.F., C.B., P.M., A.C-R., C.S., N. E. and G. M. performed experiments. Á.F.F., M.M.R.S. and G. M. participated in the generation, analysis, and maintenance of mice. A.A. performed histological analyses. G. M. wrote the manuscript. C. L-O. and G. M. devised the concept and supervised the project.

REFERENCES

1. Kuma A, Komatsu M, and Mizushima N. Autophagy-monitoring and autophagy-deficient mice. *Autophagy.* 2017;13(10):1619-28.
2. Marino G, Madeo F, and Kroemer G. Autophagy for tissue homeostasis and neuroprotection. *Current opinion in cell biology.* 2011;23(2):198-206.
3. Rubinsztein DC, Marino G, and Kroemer G. Autophagy and aging. *Cell.* 2011;146(5):682-95.
4. Numan MS, Brown JP, and Michou L. Impact of air pollutants on oxidative stress in common autophagy-mediated aging diseases. *International journal of environmental research and public health.* 2015;12(2):2289-305.
5. Lopez-Otin C, Blasco MA, Partridge L, Serrano M, and Kroemer G. The hallmarks of aging. *Cell.* 2013;153(6):1194-217.
6. Lopez-Otin C, Blasco MA, Partridge L, Serrano M, and Kroemer G. Hallmarks of aging: An expanding universe. *Cell.* 2023;186(2):243-78.
7. Fernandez AF, and Lopez-Otin C. The functional and pathologic relevance of autophagy proteases. *J Clin Invest.* 2015;125(1):33-41.
8. Tanida I, Sou YS, Ezaki J, Minematsu-Ikeguchi N, Ueno T, and Kominami E. HsAtg4B/HsApg4B/autophagin-1 cleaves the carboxyl termini of three human Atg8 homologues and delipidates microtubule-associated protein light chain 3- and GABAA receptor-associated protein-phospholipid conjugates. *J Biol Chem.* 2004;279(35):36268-76.
9. Marino G, Uria JA, Puente XS, Quesada V, Bordallo J, and Lopez-Otin C. Human autophagins, a family of cysteine proteinases potentially implicated in cell degradation by autophagy. *J Biol Chem.* 2003;278(6):3671-8.
10. Kirisako T, Ichimura Y, Okada H, Kabeya Y, Mizushima N, Yoshimori T, et al. The reversible modification regulates the membrane-binding state of Apg8/Aut7 essential for autophagy and the cytoplasm to vacuole targeting pathway. *J Cell Biol.* 2000;151(2):263-76.
11. Tamargo-Gomez I, Martinez-Garcia GG, Suarez MF, Rey V, Fueyo A, Codina-Martinez H, et al. ATG4D is the main ATG8 delipidating enzyme in mammalian cells and protects against cerebellar neurodegeneration. *Cell Death Differ.* 2021;28(9):2651-72.
12. Tamargo-Gomez I, Martinez-Garcia GG, Suarez MF, Mayoral P, Bretones G, Astudillo A, et al. Analysis of ATG4C function in vivo. *Autophagy.* 2023;19(11):2912-33.
13. Cabrera S, Marino G, Fernandez AF, and Lopez-Otin C. Autophagy, proteases and the sense of balance. *Autophagy.* 2010;6(7):961-3.
14. Cabrera S, Fernandez AF, Marino G, Aguirre A, Suarez MF, Espanol Y, et al. ATG4B/autophagin-1 regulates intestinal homeostasis and protects mice from experimental colitis. *Autophagy.* 2013;9(8):1188-200.
15. Aguirre A, Lopez-Alonso I, Gonzalez-Lopez A, Amado-Rodriguez L, Batalla-Solis E, Astudillo A, et al. Defective autophagy impairs ATF3 activity and worsens lung injury during endotoxemia. *J Mol Med (Berl).* 2014;92(6):665-76.
16. Cabrera S, Fernandez AF, Marino G, Aguirre A, Suarez MF, Espanol Y, et al. ATG4B/autophagin-1 regulates intestinal homeostasis and protects mice from experimental colitis. *Autophagy.* 2013;9(8):1188-200.
17. Cabrera S, Maciel M, Herrera I, Nava T, Vergara F, Gaxiola M, et al. Essential role for the ATG4B protease and autophagy in bleomycin-induced pulmonary fibrosis. *Autophagy.* 2015;11(4):670-84.

18. Fernandez AF, Barcena C, Martinez-Garcia GG, Tamargo-Gomez I, Suarez MF, Pietrocola F, et al. Autophagy couteracts weight gain, lipotoxicity and pancreatic beta-cell death upon hypercaloric pro-diabetic regimens. *Cell death & disease.* 2017;8(8):e2970.

19. Martinez-Garcia GG, Perez RF, Fernandez AF, Durand S, Kroemer G, and Marino G. Autophagy Deficiency by Atg4B Loss Leads to Metabolomic Alterations in Mice. *Metabolites.* 2021;11(8).

20. Rodriguez-Muela N, Germain F, Marino G, Fitze PS, and Boya P. Autophagy promotes survival of retinal ganglion cells after optic nerve axotomy in mice. *Cell Death Differ.* 2012;19(1):162-9.

21. Marino G, Fernandez AF, Cabrera S, Lundberg YW, Cabanillas R, Rodriguez F, et al. Autophagy is essential for mouse sense of balance. *The Journal of clinical investigation.* 2010;120(7):2331-44.

22. Luhr M, Saetre F, and Engedal N. The Long-lived Protein Degradation Assay: an Efficient Method for Quantitative Determination of the Autophagic Flux of Endogenous Proteins in Adherent Cell Lines. *Bio Protoc.* 2018;8(9):e2836.

23. Parfitt AM, Drezner MK, Glorieux FH, Kanis JA, Malluche H, Meunier PJ, et al. Bone histomorphometry: standardization of nomenclature, symbols, and units. Report of the ASBMR Histomorphometry Nomenclature Committee. *J Bone Miner Res.* 1987;2(6):595-610.

24. Schumacher B, van der Pluijm I, Moorhouse MJ, Kosteas T, Robinson AR, Suh Y, et al. Delayed and accelerated aging share common longevity assurance mechanisms. *PLoS Genet.* 2008;4(8):e1000161.

25. Osorio FG, Navarro CL, Cadinanos J, Lopez-Mejia IC, Quiros PM, Bartoli C, et al. Splicing-directed therapy in a new mouse model of human accelerated aging. *Sci Transl Med.* 2011;3(106):106ra7.

26. van der Pluijm I, Garinis GA, Brandt RM, Gorgels TG, Wijnhoven SW, Diderich KE, et al. Impaired genome maintenance suppresses the growth hormone--insulin-like growth factor 1 axis in mice with Cockayne syndrome. *PLoS Biol.* 2007;5(1):e2.

27. Ortega-Molina A, Lebrero-Fernandez C, Sanz A, Calvo-Rubio M, Deleyto-Seldas N, de Prado-Rivas L, et al. A mild increase in nutrient signaling to mTORC1 in mice leads to parenchymal damage, myeloid inflammation and shortened lifespan. *Nat Aging.* 2024;4(8):1102-20.

28. Lasry A, and Ben-Neriah Y. Senescence-associated inflammatory responses: aging and cancer perspectives. *Trends Immunol.* 2015;36(4):217-28.

29. De Cecco M, Ito T, Petrashen AP, Elias AE, Skvir NJ, Criscione SW, et al. L1 drives IFN in senescent cells and promotes age-associated inflammation. *Nature.* 2019;566(7742):73-8.

30. Shvets E, Fass E, and Elazar Z. Utilizing flow cytometry to monitor autophagy in living mammalian cells. *Autophagy.* 2008;4(5):621-8.

31. Abreu S, Kriegenburg F, Gomez-Sanchez R, Mari M, Sanchez-Wandelmer J, Skytte Rasmussen M, et al. Conserved Atg8 recognition sites mediate Atg4 association with autophagosomal membranes and Atg8 deconjugation. *EMBO Rep.* 2017;18(5):765-80.

32. Klionsky DJ, Abdel-Aziz AK, Abdelfatah S, Abdellatif M, Abdoli A, Abel S, et al. Guidelines for the use and interpretation of assays for monitoring autophagy (4th edition)(1). *Autophagy.* 2021;17(1):1-382.

33. Luhr M, Szalai P, and Engedal N. The Lactate Dehydrogenase Sequestration Assay - A Simple and Reliable Method to Determine Bulk Autophagic Sequestration Activity in Mammalian Cells. *J Vis Exp.* 2018(137).

34. Itakura E, and Mizushima N. Characterization of autophagosome formation site by a hierarchical analysis of mammalian Atg proteins. *Autophagy.* 2010;6(6):764-76.

35. Yamamoto H, Zhang S, and Mizushima N. Autophagy genes in biology and disease. *Nat Rev Genet.* 2023;24(6):382-400.

36. Koyama-Honda I, Itakura E, Fujiwara TK, and Mizushima N. Temporal analysis of recruitment of mammalian ATG proteins to the autophagosome formation site. *Autophagy.* 2013;9(10):1491-9.

37. Marino G, Fernandez AF, Cabrera S, Lundberg YW, Cabanillas R, Rodriguez F, et al. Autophagy is essential for mouse sense of balance. *Journal of Clinical Investigation.* 2010;120(7):2331-44.

38. Itakura E, Kishi-Itakura C, and Mizushima N. The hairpin-type tail-anchored SNARE syntaxin 17 targets to autophagosomes for fusion with endosomes/lysosomes. *Cell.* 2012;151(6):1256-69.

39. Ezaki J, Matsumoto N, Takeda-Ezaki M, Komatsu M, Takahashi K, Hiraoka Y, et al. Liver autophagy contributes to the maintenance of blood glucose and amino acid levels. *Autophagy.* 2011;7(7):727-36.

40. Harkema L, Youssef SA, and de Bruin A. Pathology of Mouse Models of Accelerated Aging. *Vet Pathol.* 2016;53(2):366-89.

41. Marino G, Ugalde AP, Fernandez AF, Osorio FG, Fueyo A, Freije JMP, et al. Insulin-like growth factor 1 treatment extends longevity in a mouse model of human premature aging by restoring somatotroph axis function. *Proceedings of the National Academy of Sciences of the United States of America.* 2010;107(37):16268-73.

42. Garinis GA, van der Horst GT, Vijg J, and Hoeijmakers JH. DNA damage and ageing: new-age ideas for an age-old problem. *Nat Cell Biol.* 2008;10(11):1241-7.

43. Marino G, Ugalde AP, Salvador-Montoliu N, Varela I, Quiros PM, Cadinanos J, et al. Premature aging in mice activates a systemic metabolic response involving autophagy induction. *Human Molecular Genetics.* 2008;17(14):2196-211.

44. Niedernhofer LJ, Garinis GA, Raams A, Lalai AS, Robinson AR, Appeldoorn E, et al. A new progeroid syndrome reveals that genotoxic stress suppresses the somatotroph axis. *Nature.* 2006;444(7122):1038-43.

45. Barcena C, Quiros PM, Durand S, Mayoral P, Rodriguez F, Caravia XM, et al. Methionine Restriction Extends Lifespan in Progeroid Mice and Alters Lipid and Bile Acid Metabolism. *Cell Rep.* 2018;24(9):2392-403.

46. Lopez-Mejia IC, de Toledo M, Chavey C, Lapasset L, Cavelier P, Lopez-Herrera C, et al. Antagonistic functions of LMNA isoforms in energy expenditure and lifespan. *EMBO Rep.* 2014;15(5):529-39.

47. Schefer V, and Talan MI. Oxygen consumption in adult and AGED C57BL/6J mice during acute treadmill exercise of different intensity. *Exp Gerontol.* 1996;31(3):387-92.

48. Penn DJ, Zala SM, and Luzynski KC. Regulation of Sexually Dimorphic Expression of Major Urinary Proteins. *Front Physiol.* 2022;13:822073.

49. Garratt M, Stockley P, Armstrong SD, Beynon RJ, and Hurst JL. The scent of senescence: sexual signalling and female preference in house mice. *J Evol Biol.* 2011;24(11):2398-409.

50. Yan J, Gao Y, Bai J, Li J, Li M, Liu X, et al. SERPINB1 promotes Senecavirus A replication by degrading IKBKE and regulating the IFN pathway via autophagy. *J Virol.* 2023;97(10):e0104523.

51. Barnhoorn S, Meima ME, Peeters RP, Darras VM, Leeuwenburgh S, Hoeijmakers JHJ, et al. Decreased hepatic thyroid hormone signaling in systemic and liver-specific but not brain-specific accelerated aging due to DNA repair deficiency in mice. *Eur Thyroid J.* 2023;12(6).

52. Wiechert L, Nemeth J, Pusterla T, Bauer C, De Ponti A, Manthey S, et al. Hepatocyte-specific S100a8 and S100a9 transgene expression in mice causes Cxcl1 induction and systemic neutrophil enrichment. *Cell Commun Signal.* 2012;10(1):40.

53. Gupta U, Ghosh S, Wallace CT, Shang P, Xin Y, Nair AP, et al. Increased LCN2 (lipocalin 2) in the RPE decreases autophagy and activates inflammasome-ferroptosis processes in a mouse model of dry AMD. *Autophagy.* 2023;19(1):92-111.

54. Asimakopoulou A, Weiskirchen S, and Weiskirchen R. Lipocalin 2 (LCN2) Expression in Hepatic Malfunction and Therapy. *Front Physiol.* 2016;7:430.

55. Carrero D, Soria-Valles C, and Lopez-Otin C. Hallmarks of progeroid syndromes: lessons from mice and reprogrammed cells. *Dis Model Mech.* 2016;9(7):719-35.

56. Collado M, Blasco MA, and Serrano M. Cellular senescence in cancer and aging. *Cell.* 2007;130(2):223-33.

57. Kauffman KJ, Yu S, Jin J, Mugo B, Nguyen N, O'Brien A, et al. Delipidation of mammalian Atg8-family proteins by each of the four ATG4 proteases. *Autophagy.* 2018;14(6):992-1010.

58. Nguyen TN, Padman BS, Zellner S, Khuu G, Uoselis L, Lam WK, et al. ATG4 family proteins drive phagophore growth independently of the LC3/GABARAP lipidation system. *Mol Cell.* 2021;81(9):2013-30 e9.

59. Agrotis A, Pengo N, Burden JJ, and Ketteler R. Redundancy of human ATG4 protease isoforms in autophagy and LC3/GABARAP processing revealed in cells. *Autophagy.* 2019;15(6):976-97.

60. Nguyen N, Olivas TJ, Mires A, Jin J, Yu S, Luan L, et al. The insufficiency of ATG4A in macroautophagy. *J Biol Chem.* 2020;295(39):13584-600.

61. Grunwald DS, Otto NM, Park JM, Song D, and Kim DH. GABARAPs and LC3s have opposite roles in regulating ULK1 for autophagy induction. *Autophagy.* 2020;16(4):600-14.

62. Ramirez-Pardo I, Villarejo-Zori B, Jimenez-Loygorri JI, Sierra-Filardi E, Alonso-Gil S, Marino G, et al. Ambra1 haploinsufficiency in CD1 mice results in metabolic alterations and exacerbates age-associated retinal degeneration. *Autophagy.* 2023;19(3):784-804.

FIGURE LEGENDS

Figure 1. Generation of *atg4b*$^{-/-}$*atg4c*$^{-/-}$*atg4d*$^{-/-}$ (ATG4A-only) mice. (A) Schematic representations of wild-type locus for *Atg4b*, *Atg4c* and *Atg4d* genes (with coding exons represented as black boxes) showing the different gene targeting strategies to disrupt the transcription of each gene. **(B)** PCR analysis of genomic DNA from a WT control mouse (lane 1), a heterozygous control mouse (lane 2), different *Atg4* knock-out control mice (lane 3, for each gene) and an ATG4A-only mouse (lane 4). **(C)** RT-qPCR analysis of kidney tissue RNA from WT and ATG4A-only mice confirming the absence of *Atg4b*, *Atg4c* and *Atg4d* expression. **(D)** Representative immunoblots of ATG4A in extracts from control and mutant mice kidneys. **(E)** Size comparison of WT and ATG4-only neonates and 2-month-old adult mice. LOAD: β-actin. Bars represent means ± SD (N > 3 mice per genotype, at least 3 independent experiments). *, $P < 0.05$; **, $P < 0.01$; 2-tailed unpaired Student's t-test.

Figure 2. Characterization of the autophagic response in ATG4A-only cells. (A) Representative immunoblotting of mATG8 proteins and autophagy substrates in protein extracts from WT and ATG4A-only MEFs upon autophagy induction with EBSS medium and/or autophagy inhibition with bafilomycin A1 (BafA1) treatment. *, uncleaved pro-GABARAPL1 protein. **(B)** Representative images of immunofluorescence analysis of endogenous mATG8 proteins in WT and ATG4A-only MEFs. **(C)** Quantification of the data from (B). **(D)** Representative immunoblotting of protein extracts from WT, *Atg4b*-deficient and ATG4A-only MEFs that were transfected with mammalian expression vectors containing tagged cDNAs of LC3A, LC3B, GABARAP, GABARAPL1 and GABARAPL2. **(E)** Representative immunoblotting of p62 and ubiquitinated proteins in protein extracts from WT and ATG4A-only MEFS after being cultured in EBSS for the indicated times. **(F)** Quantification of the data from (E). **(G)** Representative images and analysis of p62-positive structures in WT and ATG4-only MEFs stably expressing GFP-p62. **(H)** Representative flow cytometry profiles for GFP-LC3B degradation in response to nutrient deprivation in the presence/absence of BafA1 in WT and ATG4A-only MEFs. LOAD: β-actin. Bars represent means ± SEM (C, G) and ± SD (F). (N > 3 independent experiments). *, $P < 0.05$; 2-tailed unpaired Student's t-test. Scale bars: 10 μm.

Figure 3. Autophagy and proteolysis regulation in ATG4A-only cells. (A) Representative fluorescence microscope images (left) and statistical analyses (right) of WT and ATG4-only MEFs stably expressing GFP-LC3B upon nutrient deprivation and/or BafA1 treatment. **(B)** Representative immunofluorescence images of endogenous SQSTM1/p62 and Ubiquitin in WT and ATG4A-only MEFs stably expressing GFP-LC3B, showing the presence of p62- and Ubiquitin-positive protein aggregates containing GFP-LC3B. **(C)** Representative immunoblotting (left) and quantitation (right) of LC3B after performing a proteinase K protection assay in WT and ATG4A-only MEFs in control or nutrient deprivation conditions (C, control; PK, proteinase K; T, Triton X-100; PK, proteinase K + Triton X-100). **(D)** Lactate dehydrogenase (LDH) sequestration

and long-live protein degradation (SAR405- and BafA1-sensitive) assays in WT and ATG4A-only MEFs. **(E)** Representative images of WT and ATG4A-only MEFs stably expressing GFP-WIPI1, GFP-DFCP1, GFP-ATG13, GFP-STX17 and GFP-VAMP8 in response to nutrient deprivation in the presence/absence of BafA1. **(F)** Quantitation of the data from (E). **(G)** Representative immunoblotting images of components of the ULK1-complex (ULK1, FIP200, ATG13 and ATG101) and ATG14 in WT and ATG4A-only MEFs upon nutrient deprivation. **(H)** Representative images of WT and ATG4A-only MEFs stably expressing GFP-ATG5 and cultured in regular or starvation medium for 4 hours (left) and the quantification of the data from the autophagy-inducing condition (right). **(I)** Representative images and analysis of WT and ATG4-only MEFs stably expressing GFP-p62 after inducing the formation of protein aggregates by puromycin treatments for the indicated times. **(J)** Left, quantification of cells with aggregates after 9 hours of puromycin treatment upon nutrient deprivation and/or BafA1 treatment. Right, cell survival analysis of WT and ATG4A-only MEFs after the treatment with puromycin. LOAD: β-actin. Bars represent means ± SEM (N > 3 independent experiments). *, $P < 0.05$; 2-tailed unpaired Student's t-test. Scale bars: 10 µm.

Figure 4: Autophagy alterations in ATG4A-only mice. (A) Representative immunoblots of endogenous mATG8 proteins, p62 and LAMP1 in extracts from WT and ATG4A-only mice. *, uncleaved GABARAPL1 protein. **(B)** Representative immunofluorescence images (left) and quantification (right) of endogenous mATG8s in muscle and liver from WT and ATG4A-only mice. **(C)** Representative immunohistochemistry images of endogenous SQSTM1/p62 in tissues from WT and ATG4A-only mice. **(D)** Representative immunoblotting images of components of the ULK1-complex (ULK1, FIP200, ATG13 and ATG101) and ATG14 in WT and ATG4A-only mice liver tissue extracts. LOAD: β-actin. Bars represent means ± SEM (N > 3 mice per genotype, at least 3 independent experiments). *, $P < 0.05$; 2-tailed unpaired Student's t-test. Scale bars: 10 µm (B) and 50 µm (C).

Figure 5: Characterization of ATG4A-only mice. (A) Weight comparison between WT and ATG4A-only male and female mice. **(B)** Survival comparison of WT and ATG4A-only mice colonies. **(C)** Representative H&E images of the inner ear of WT and ATG4A-only mice, showing alterations in otoconial development. **(D)** Representative limb postures responding to tail suspension in WT and ATG4A-only mice. **(E)** Representative paw placement records of WT and ATG4A-only mice after footprint pattern analysis. **(F)** Performance on the raised-beam (measured by the time mice spent before reaching the end of the beam) and grip strength (measured by the time mice were able to hold themselves to a grid when inverted) tests in WT and ATG4A-only mice. **(G)** Results from Rotarod analyses of WT and ATG4A-only mice. **(H-K)** Quantification of the levels of platelets (H), granulocytes (I), hematocrit (J) and lymphocytes (K) in blood samples from WT and ATG4A-only mice. Bars represent means ± SD (N > 6 mice per genotype, at least 3 independent experiments). *, $P < 0.05$; 2-tailed unpaired Student's t-test. Scale bar: 50 µm.

Figure 6: Organ-specific and biochemical alterations in ATG4A-only mice. (A) Representative images of H&E (skin, brown adipose tissue, spleen and colon) and Gomori trichrome (kidney, lung, heart) and anti-insulin IHC (pancreas) stainings of tissues from WT and ATG4A-only mice (arrows represent damaged/fibrotic areas). Scale bars: 200 µm (lung, spleen, colon, scapular fat, pancreas, and kidney), and 500 µm (kidney heart). **(B)** Representative images and analysis of bones from WT and ATG4A-only mice, showing the quantification for morphometric parameters like the percentage of bone volume (ratio bone volume/tissue volume), the trabecular number, the connectivity density among trabeculae and the bone mineral density. **(C)** Quantification of major biochemical parameters (including cholesterol, triglycerides, bile acids, hepatic aminotransferases and amylase) in blood samples from WT and ATG4A-only mice. **(D)** Quantification of hormonal parameters (including IGF-1, growth hormone, insulin, leptin and adiponectin) in blood samples from WT and ATG4A-only mice. **(E)** Representative images of periodic acid-Schiff (PAS) staining in livers from WT and ATG4A-only mice showing hepatic glycogen accumulation in mutant animals Scale bars: 50 µm. **(F)** Analysis of O_2 consumption and CO_2 production by WT and ATG4A-only mice. Bars represent means ± SD (N > 6 mice per genotype, at least 3 independent experiments). *, $P < 0.05$; 2-tailed unpaired Student's t-test.

Figure 7. Transcriptomic analysis of ATG4A-only mice. A) Heatmap displaying gene expression of the top differentially expressed genes in liver ATG4A-only compared to WT mice. Significant genes were filtered to capture those with an absolute $\log_2$FC value greater than 2, and the top 50 genes with the lower adjusted p-value were selected for representation. **B)** Gene expression signatures significantly altered in ATG4A-only liver transcriptome. GSEA was performed using gene sets from MSigDB and gene expression data from progeroid model studies. Circle size and color correlate with the -$\log_{10}$ adjusted p-value of the analysis. **C)** MA plot showing the differential expression analysis of ATG4A-only versus WT liver mouse transcriptomes. The names of the top 20 genes with the lower adjusted p-value are indicated in the plot along with the direction of their change. **D)** Western blot analysis of MUPs, LCN2 and S100a9 protein levels in WT and ATG4A-only liver. GAPDH protein levels are shown as loading control. **E)** Heatmap of genes in the leading edge of GSEA analysis against previously published progeroid transcriptional profiles. The upper panel shows the genes enriched in the "Upregulated genes in *ERCC*$^{-/\Delta 7}$ mice" signature, whilst the bottom panel shows the genes enriched in the "Downregulated genes in *Lmna*$^{G609G/G609G}$ mice" signature. **F)** Running score plots of GSEA of liver ATG4A-only transcriptomic profile against MSigDB signatures of fatty acid metabolism (left), inflammatory response (middle) and interferon-gamma response (right).

Figure 8: ATG4 deficiency leads to accelerated aging. (A) Representative immunoblots of markers of DNA damage and DNA damage response (DDR) in tissues from WT and ATG4A-only mice. **(B)** Left, representative images of senescence-associated beta-galactosidase (SA-β-Gal) staining, p21 immunohistochemistry (middle) and its quantification (right) in livers from WT and ATG4A-only mice. **(C)** Senescence-related gene expression signatures significantly altered in ATG4A-only liver transcriptome. SASP and IFN-1 genesets were obtained from (29) and SIR geneset from (28). Circle size and colour correlate with the $-\log_{10}$ adjusted p-value of the analysis. **(D)** Survival analysis of WT, *atg4b*$^{-/-}$, *atg4b*$^{-/-}$ *atg4c*$^{-/-}$ and *atg4b*$^{-/-}$ *atg4d*$^{-/-}$ and ATG4A-only mice colonies. **(E)** Mean, median and maximal survival values for each colony. **(F)** Statistical analysis (Log-rank Mantel-Cox test) for every possible comparison between colonies. LOAD: GAPDH. Bars represent means ± SD (N > 3 mice per genotype). *, $P < 0.05$; 2-tailed unpaired Student's t-test. Scale bar: 50 µm.

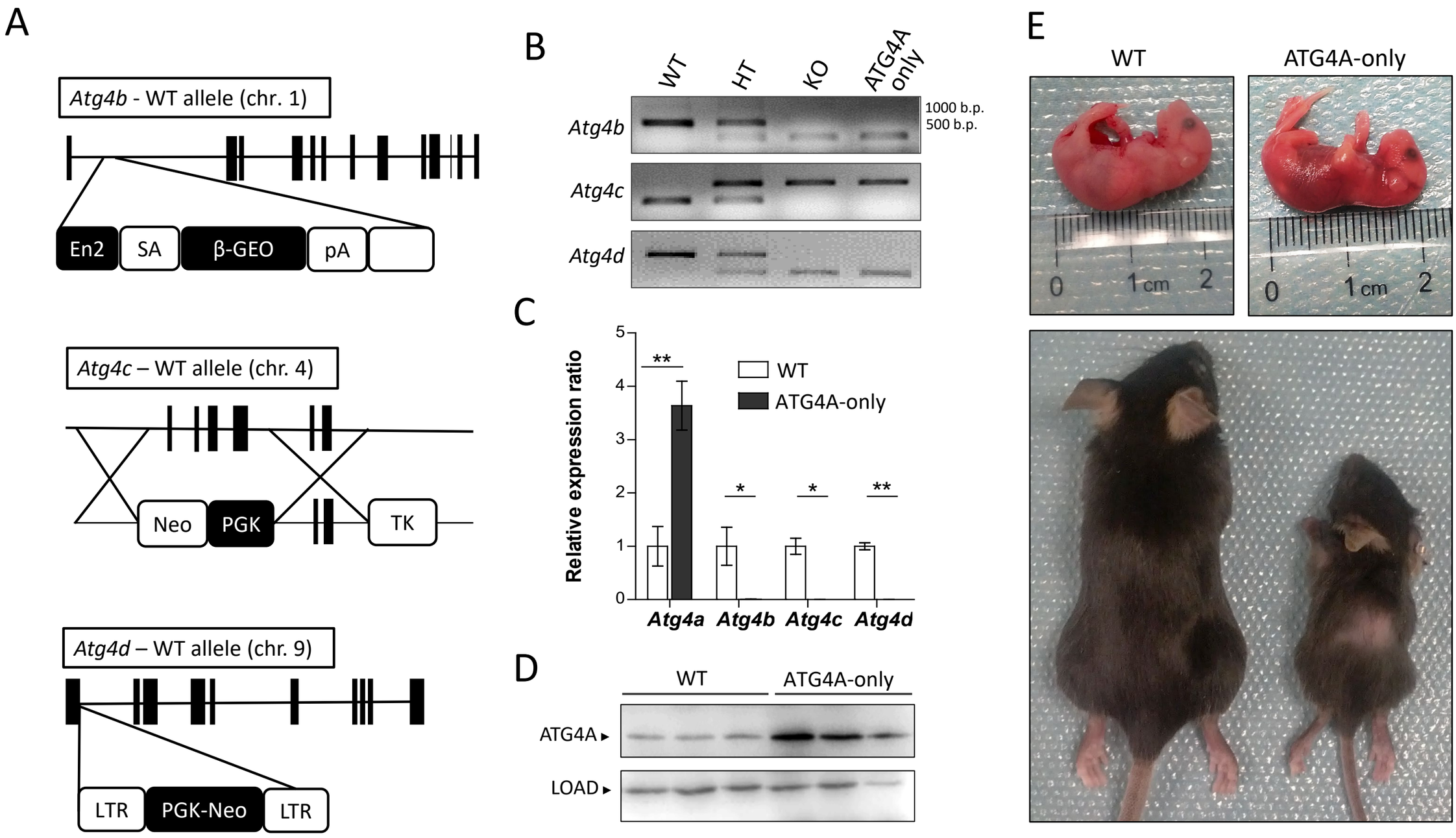
A
Atg4b - WT allele (chr. 1)
En2
SA
β-GEO
pA
Atg4c – WT allele (chr. 4)
Neo
PGK
TK
Atg4d – WT allele (chr. 9)
LTR
PGK-Neo
LTR
B
WT
HT
KO
ATG4A only
Atg4b
Atg4c
Atg4d
1000 b.p.
500 b.p.
C
Relative expression ratio
WT
ATG4A-only
Atg4a
Atg4b
Atg4c
Atg4d
D
WT
ATG4A-only
ATG4A
LOAD
E
WT
ATG4A-only
0
1 cm
2

Figure 1

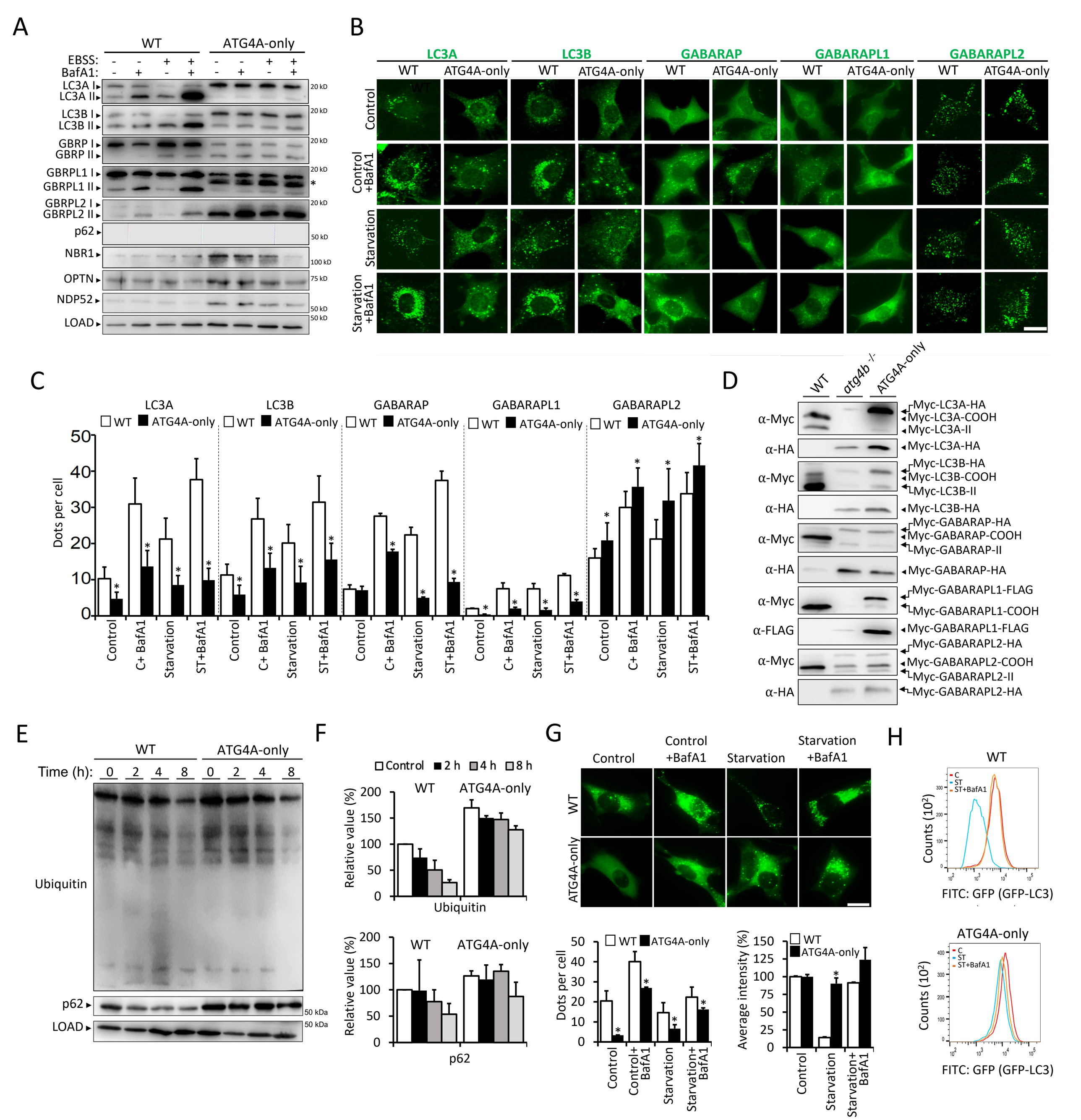
A
WT
ATG4A-only
EBSS:
BafA1:
LC3A I
LC3A II
LC3B I
LC3B II
GBRP I
GBRP II
GBRPL1 I
GBRPL1 II
GBRPL2 I
GBRPL2 II
p62
NBR1
OPTN
NDP52
LOAD
20 kD
50 kD
100 kD
75 kD
B
LC3A
LC3B
GABARAP
GABARAPL1
GABARAPL2
Control
Control +BafA1
Starvation
Starvation +BafA1
C
Dots per cell
D
WT
atg4b -/-
ATG4A-only
α-Myc
α-HA
α-FLAG
Myc-LC3A-HA
Myc-LC3A-COOH
Myc-LC3A-II
Myc-LC3B-HA
Myc-LC3B-COOH
Myc-LC3B-II
Myc-GABARAP-HA
Myc-GABARAP-COOH
Myc-GABARAP-II
Myc-GABARAPL1-FLAG
Myc-GABARAPL1-COOH
Myc-GABARAPL2-HA
Myc-GABARAPL2-COOH
Myc-GABARAPL2-II
E
Time (h):
Ubiquitin
p62
LOAD
F
Control
2 h
4 h
8 h
Relative value (%)
Ubiquitin
p62
G
Control
Control +BafA1
Starvation
Starvation +BafA1
Average intensity (%)
H
Counts (10²)
FITC: GFP (GFP-LC3)
C
ST
ST+BafA1

Figure 2

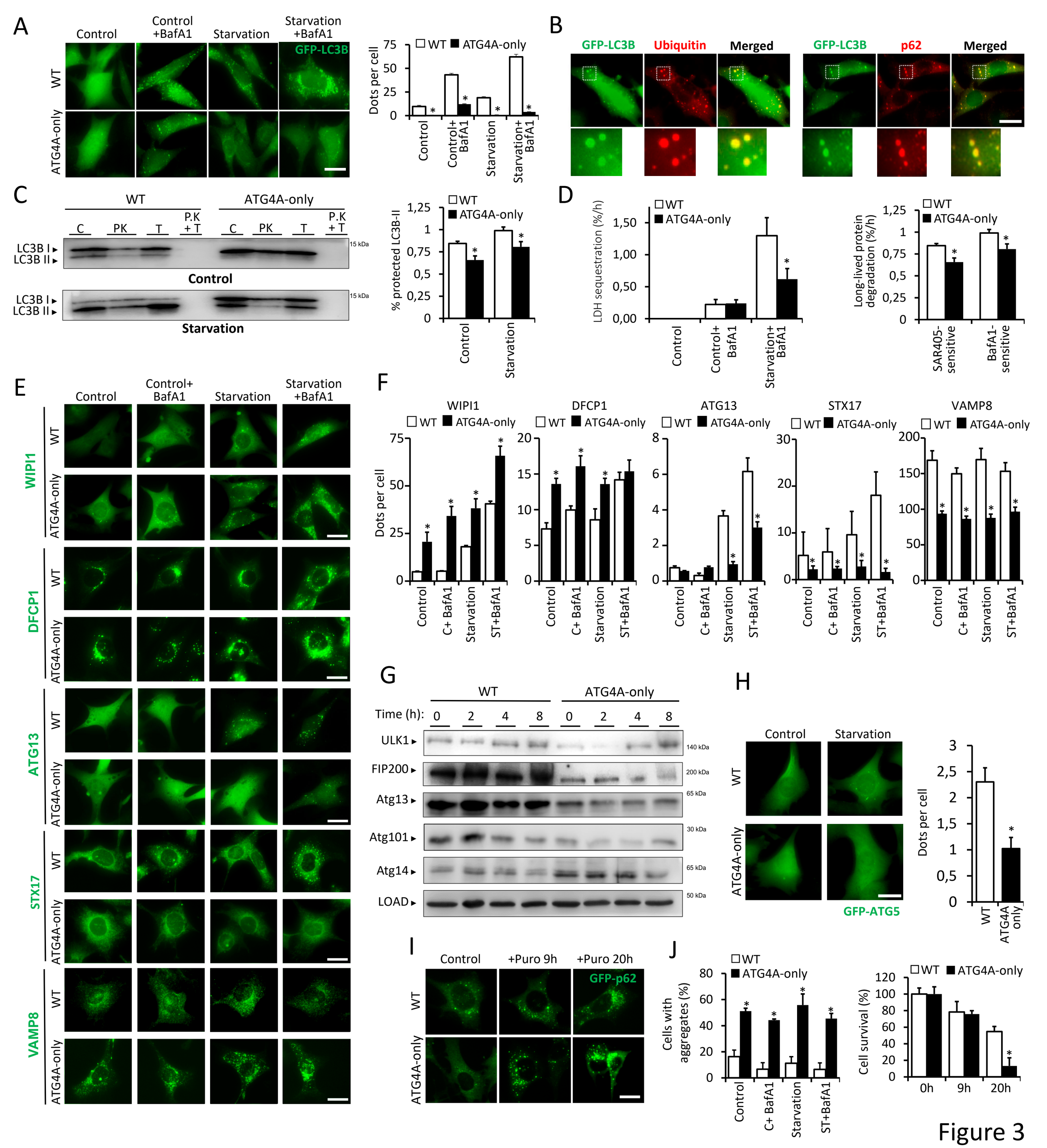
A
Control
Control +BafA1
Starvation
Starvation +BafA1
GFP-LC3B
WT
ATG4A-only
Dots per cell
WT
ATG4A-only
Control
Control+ BafA1
Starvation
Starvation+ BafA1
B
GFP-LC3B
Ubiquitin
Merged
GFP-LC3B
p62
Merged
C
WT
ATG4A-only
C
PK
T
P.K + T
LC3B I
LC3B II
15 kDa
Control
Starvation
% protected LC3B-II
D
LDH sequestration (%/h)
Long-lived protein degradation (%/h)
SAR405-sensitive
BafA1-sensitive
E
WIPI1
DFCP1
ATG13
STX17
VAMP8
F
WIPI1
DFCP1
ATG13
STX17
VAMP8
C+ BafA1
ST+BafA1
G
Time (h):
ULK1
FIP200
Atg13
Atg101
Atg14
LOAD
140 kDa
200 kDa
65 kDa
30 kDa
50 kDa
H
GFP-ATG5
I
+Puro 9h
+Puro 20h
GFP-p62
J
Cells with aggregates (%)
Cell survival (%)
0h
9h
20h

Figure 3

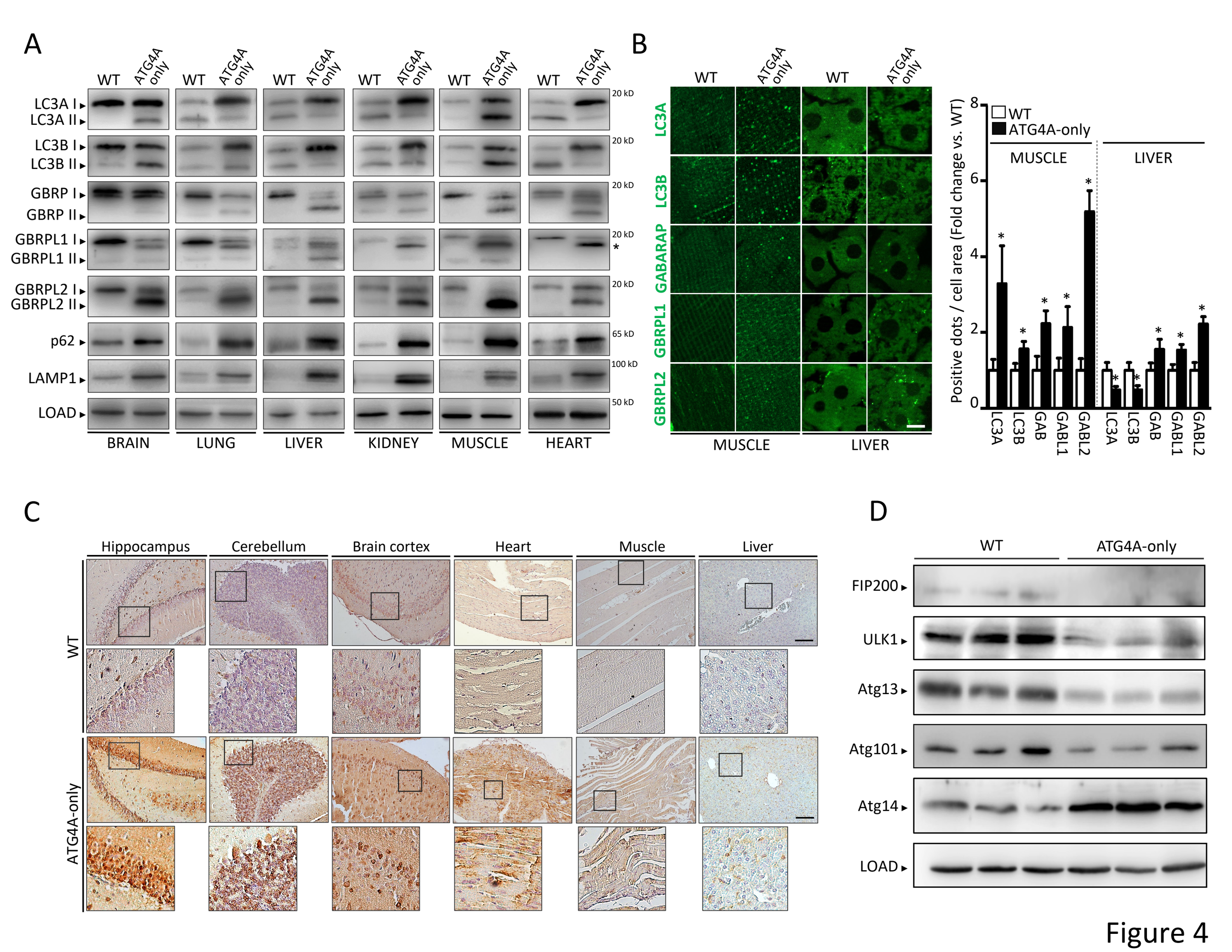
A
WT
ATG4A only
LC3A I
LC3A II
LC3B I
LC3B II
GBRP I
GBRP II
GBRPL1 I
GBRPL1 II
GBRPL2 I
GBRPL2 II
p62
LAMP1
LOAD
20 kD
65 kD
100 kD
50 kD
BRAIN
LUNG
LIVER
KIDNEY
MUSCLE
HEART
B
LC3A
LC3B
GABARAP
GBRPL1
GBRPL2
MUSCLE
LIVER
WT
ATG4A-only
Positive dots / cell area (Fold change vs. WT)
LC3A
LC3B
GAB
GABL1
GABL2
C
Hippocampus
Cerebellum
Brain cortex
Heart
Muscle
Liver
WT
ATG4A-only
D
FIP200
ULK1
Atg13
Atg101
Atg14
LOAD

Figure 4

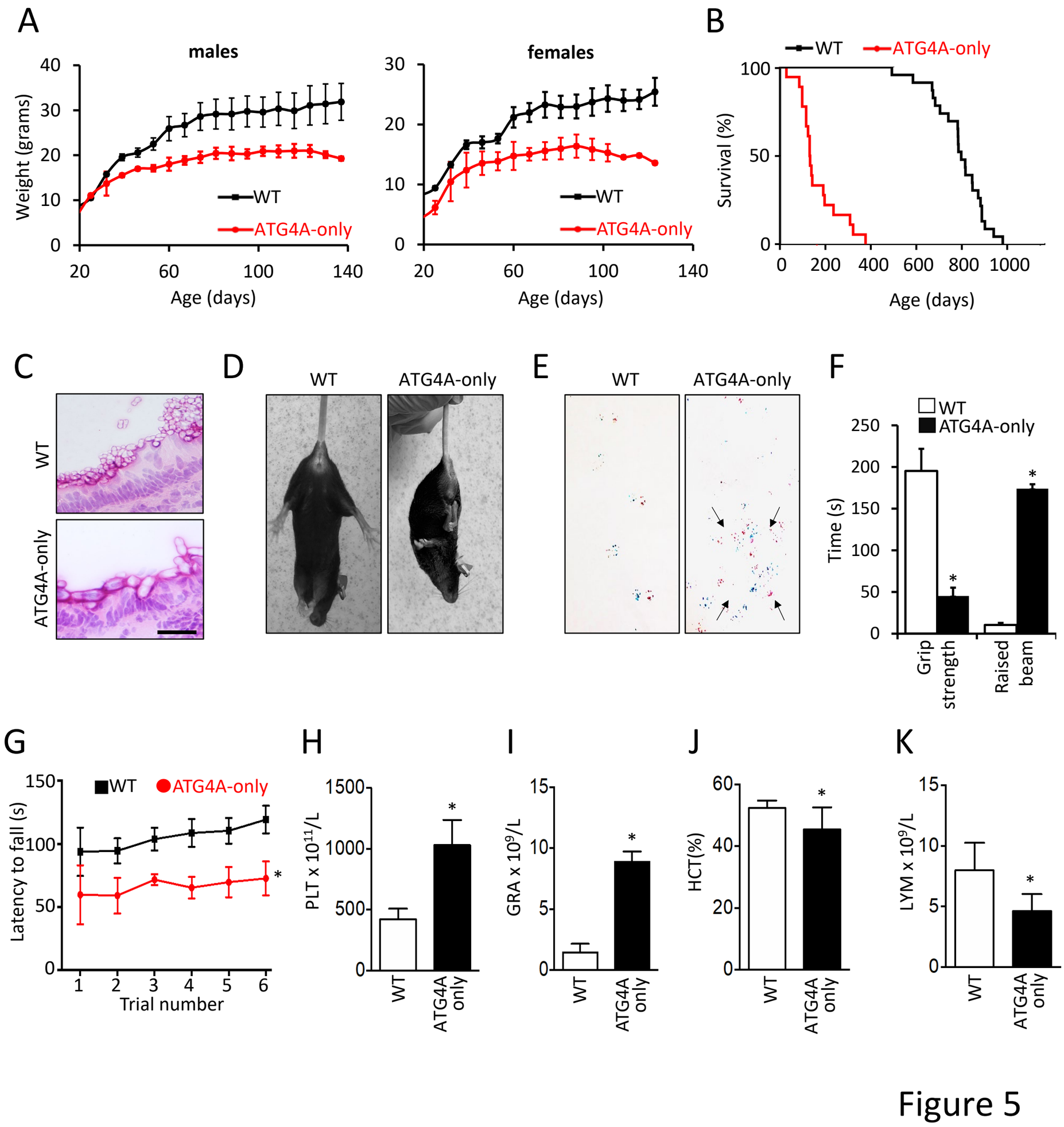
A
males
Weight (grams)
Age (days)
WT
ATG4A-only
females
B
Survival (%)
C
WT
ATG4A-only
D
E
F
Time (s)
Grip strength
Raised beam
G
Latency to fall (s)
Trial number
H
PLT x 10^11/L
I
GRA x 10^9/L
J
HCT(%)
K
LYM x 10^9/L

Figure 5

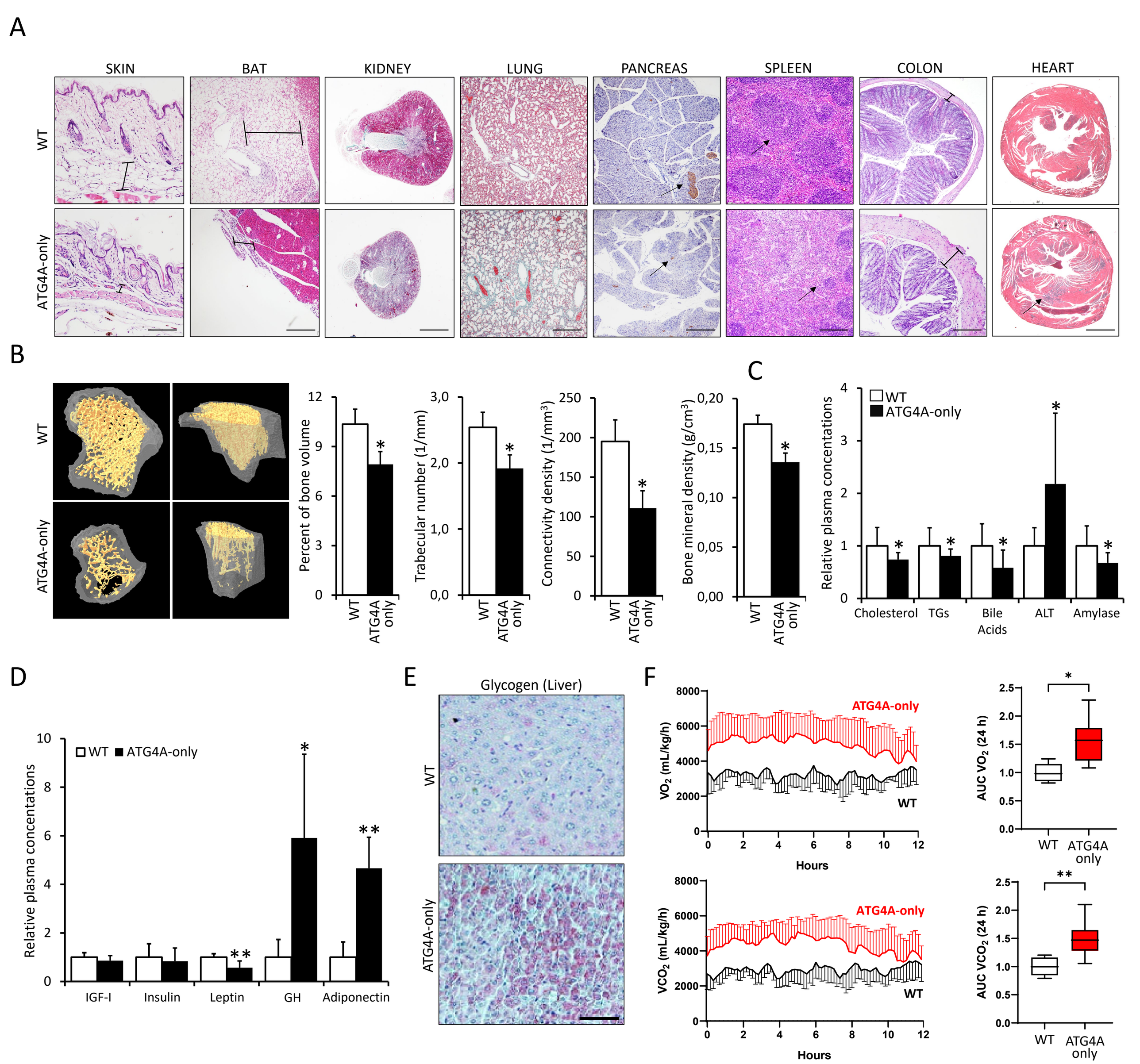
A
SKIN
BAT
KIDNEY
LUNG
PANCREAS
SPLEEN
COLON
HEART
WT
ATG4A-only
B
WT
ATG4A-only
Percent of bone volume
Trabecular number (1/mm)
Connectivity density (1/mm³)
Bone mineral density (g/cm³)
WT
ATG4A only
C
WT
ATG4A-only
Relative plasma concentations
Cholesterol
TGs
Bile Acids
ALT
Amylase
D
WT
ATG4A-only
Relative plasma concentations
IGF-I
Insulin
Leptin
GH
Adiponectin
E
Glycogen (Liver)
WT
ATG4A-only
F
ATG4A-only
WT
VO2 (mL/kg/h)
VCO2 (mL/kg/h)
Hours
AUC VO2 (24 h)
AUC VCO2 (24 h)
WT
ATG4A only

Figure 6

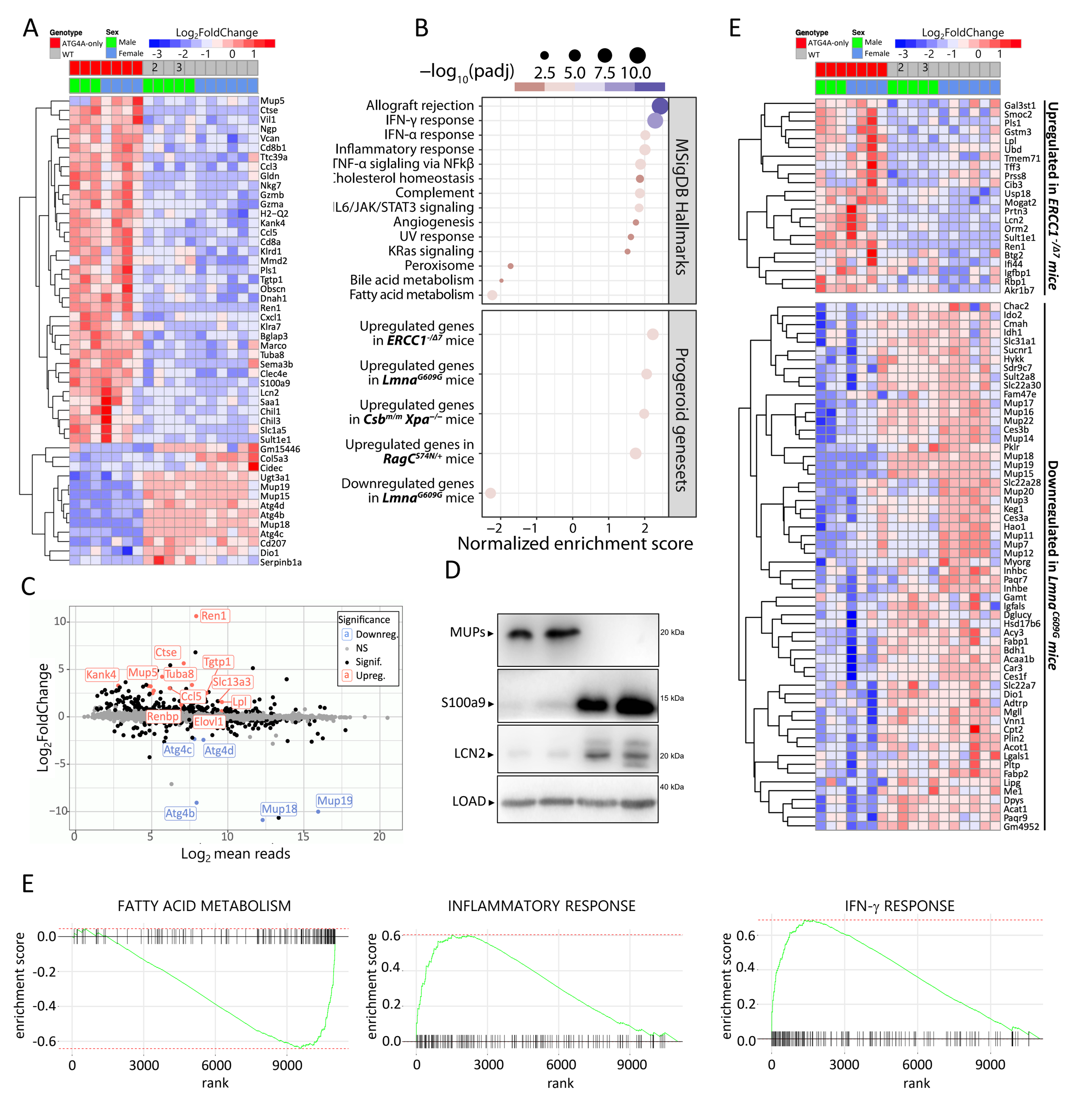
A
Genotype
ATG4A-only
WT
Sex
Male
Female
Log2FoldChange
-3 -2 -1 0 1
2 3
Mup5
Ctse
Vil1
Ngp
Vcan
Cd8b1
Ttc39a
Ccl3
Gldn
Nkg7
Gzmb
Gzma
H2-Q2
Kank4
Ccl5
Cd8a
Klrd1
Mmd2
Pls1
Tgtp1
Obscn
Dnah1
Ren1
Cxcl1
Klra7
Bglap3
Marco
Tuba8
Sema3b
Clec4e
S100a9
Lcn2
Saa1
Chil1
Chil3
Slc1a5
Sult1e1
Gm15446
Col5a3
Cidec
Ugt3a1
Mup19
Mup15
Atg4d
Atg4b
Mup18
Atg4c
Cd207
Dio1
Serpinb1a
B
–log10(padj)
2.5 5.0 7.5 10.0
Allograft rejection
IFN-γ response
IFN-α response
Inflammatory response
TNF-α siglaling via NFkβ
Cholesterol homeostasis
Complement
IL6/JAK/STAT3 signaling
Angiogenesis
UV response
KRas signaling
Peroxisome
Bile acid metabolism
Fatty acid metabolism
MSigDB Hallmarks
Upregulated genes in ERCC1-/Δ7 mice
Upregulated genes in Lmna G609G mice
Upregulated genes in Csb m/m Xpa −/− mice
Upregulated genes in RagC S74N/+ mice
Downregulated genes in Lmna G609G mice
Progeroid genesets
−2 −1 0 1 2
Normalized enrichment score
C
Significance
Downreg.
NS
Signif.
Upreg.
Ren1
Ctse
Tgtp1
Kank4
Mup5
Tuba8
Slc13a3
Ccl5
Lpl
Renbp
Elovl1
Atg4c
Atg4d
Atg4b
Mup18
Mup19
Log2FoldChange
Log2 mean reads
D
MUPs
S100a9
LCN2
LOAD
20 kDa
15 kDa
20 kDa
40 kDa
E
Gal3st1
Smoc2
Pls1
Gstm3
Lpl
Ubd
Tmem71
Tff3
Prss8
Cib3
Usp18
Mogat2
Prtn3
Lcn2
Orm2
Sult1e1
Ren1
Btg2
Ifi44
Igfbp1
Rbp1
Akr1b7
Upregulated in ERCC1-/Δ7 mice
Chac2
Ido2
Cmah
Idh1
Slc31a1
Sucnr1
Hykk
Sdr9c7
Sult2a8
Slc22a30
Fam47e
Mup17
Mup16
Mup22
Ces3b
Mup14
Pklr
Mup18
Mup19
Mup15
Slc22a28
Mup20
Mup3
Keg1
Ces3a
Hao1
Mup11
Mup7
Mup12
Myorg
Inhbc
Paqr7
Inhbe
Gamt
Igfals
Dglucy
Hsd17b6
Acy3
Fabp1
Bdh1
Acaa1b
Car3
Ces1f
Slc22a7
Dio1
Adtrp
Mgll
Vnn1
Cpt2
Plin2
Acot1
Lgals1
Pltp
Fabp2
Lipg
Me1
Dpys
Acat1
Paqr9
Gm4952
Downregulated in Lmna G609G mice
E
FATTY ACID METABOLISM
INFLAMMATORY RESPONSE
IFN-γ RESPONSE
enrichment score
rank

Figure 7

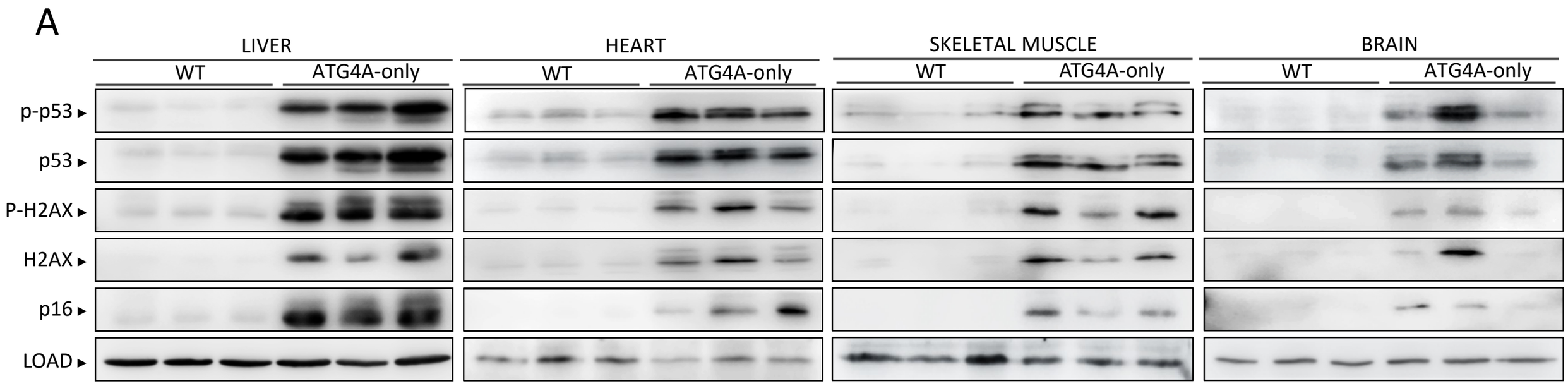

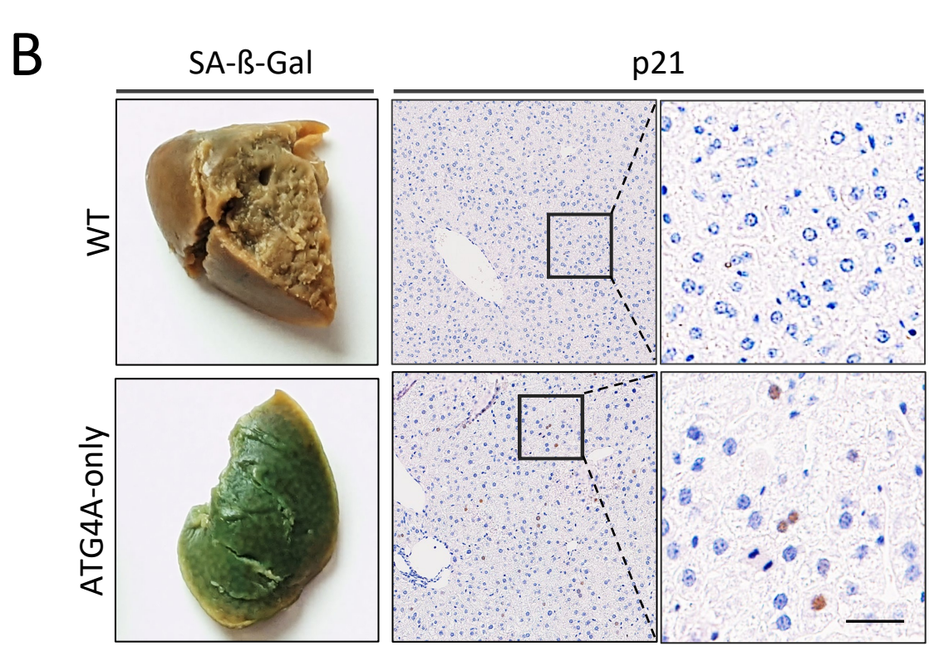

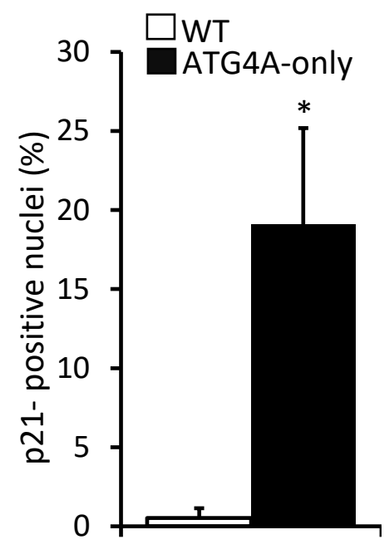

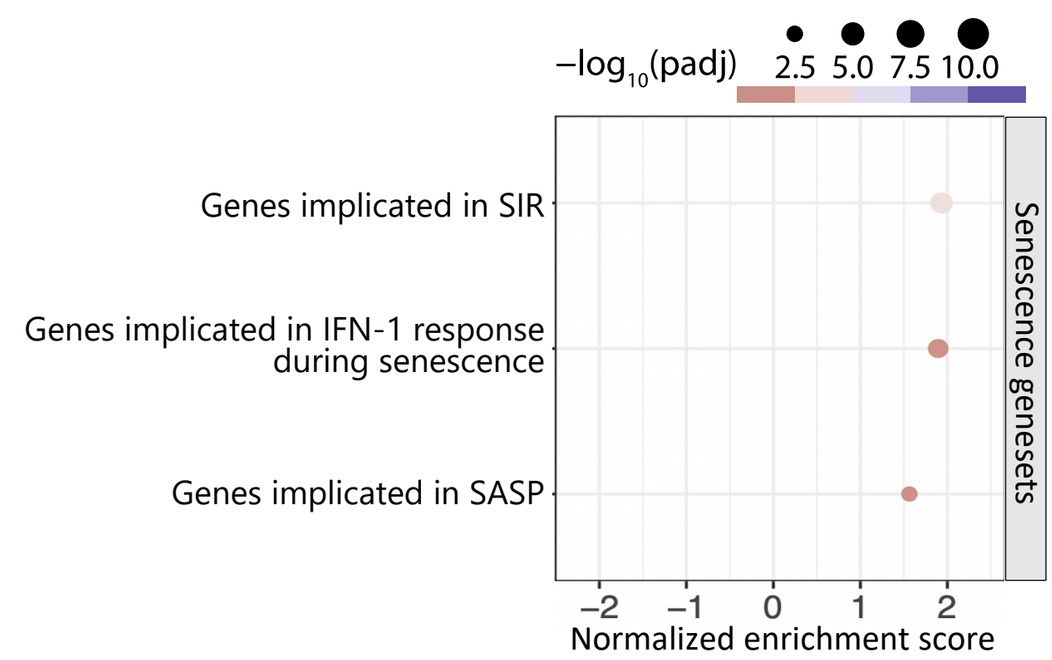

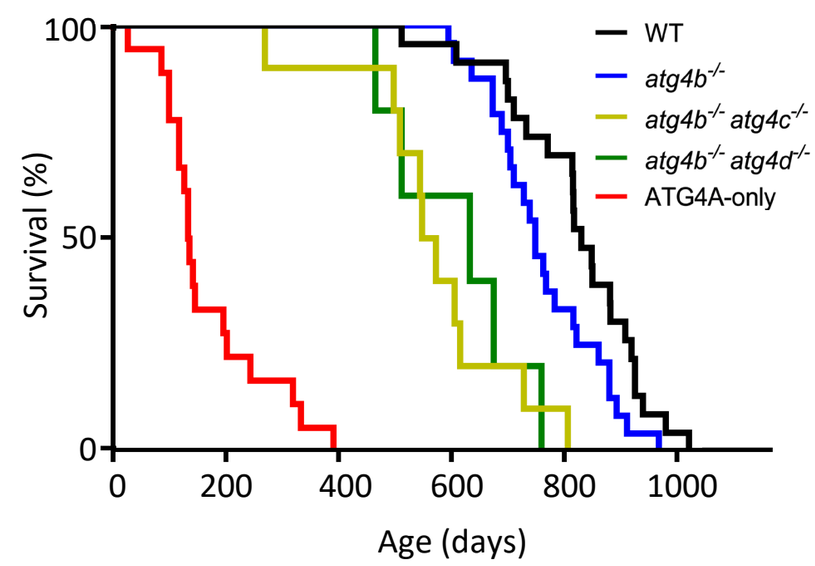

E

Survival (days)	Mean	Median	Maximal
WT	814.52	823	1012
***atg4b*$^{-/-}$**	755.38	742	959
***atg4b*$^{-/-}$ *atg4c*$^{-/-}$**	564.40	555	799
***atg4b*$^{-/-}$ *atg4d*$^{-/-}$**	603.40	627	753
ATG4A-only	167.44	133	387

F

Log-rank (Mantel-Cox)

	WT	***atg4b*$^{-/-}$**	***atg4b*$^{-/-}$ *atg4c*$^{-/-}$**	***atg4b*$^{-/-}$ *atg4d*$^{-/-}$**
***atg4b*$^{-/-}$**	0.0306			
***atg4b*$^{-/-}$ *atg4c*$^{-/-}$**	< 0.0001	0.0001		
***atg4b*$^{-/-}$ *atg4d*$^{-/-}$**	< 0.0001	0.0041	0.7535	
ATG4A-only	< 0.0001	< 0.0001	< 0.0001	0.0002

Figure 8